TITLE

Partial input loss differentially modifies neural pathways

AUTHORS

Joo Yeun Lee[1✢], David B. Kastner[2], Scott C. Harris[1], Luca Della Santina[3], Jeremiah V. John[1], Natalia S. Stone[1], and Felice A. Dunn[1✢]

AFFILIATIONS:

[1]Department of Ophthalmology
University of California, San Francisco
San Francisco, CA 94143-0518, USA

[2]Department of Psychiatry and Behavioral Sciences
University of California, San Francisco
San Francisco, CA 94143-0518, USA

[3]College of Optometry
University of Houston
Houston, TX 77204-2020, USA

Corresponding authors contacts:
✢Felice.Dunn@ucsf.edu, JooYeun.Lee@ucsf.edu

✢ Lead Contacts

ABSTRACT

Following input loss from degeneration, injury, and/or aging, downstream circuits undergo modifications that can impact neural computations. How neural computations across different pathways are affected by common input loss remain understudied. Using the retina to leverage known cell types, well-defined circuitry, and molecular tools, we show how multiple pathways adjust their functional properties differently to common input loss and further locate these changes within each pathway. Specifically, we asked if two OFF ganglion cell types, alpha OFF-sustained (A_{OFF-S}) and OFF-transient (A_{OFF-T}) cells, and their respective dominant presynaptic partners, type 2 and type 3a cone bipolar cells, respond differentially to partial cone

loss. We find that $A_{OFF\text{-}T}$ ganglion cells exhibit more circuit changes than $A_{OFF\text{-}S}$ ganglion cells, resulting in altered spatiotemporal tuning following partial cone loss. We show that the underlying mechanisms include changes in glutamatergic, GABAergic, and glycinergic circuits in the pathway of $A_{OFF\text{-}T}$ ganglion cells. In response to common input loss, our study finds different locations of circuit modifications across OFF pathways. In two OFF pathways, these distinct functional changes contribute to maintaining perceptually relevant information, preserving key visual features despite input loss. These findings provide insight into how sensory systems can compensate to ultimately serve vision.

INTRODUCTION

Across sensory systems, neuronal pathways can undergo distinct changes in response to deafferentation (Villa et al., 2016; Liu et al., 2017; Eavri et al., 2018; Karoui et al., 2023; Kumar et al., 2023). The mechanisms underlying these differential responses and their implications for potential pathway-specific repair remain open questions. Given the dynamic properties of our nervous system even when natural regeneration is not possible, achieving optimal sensory restoration through artificial intervention requires systematic examination of the states of remaining circuitry in response to deafferentation and following rescue. Our understanding of that degeneration process is severely limited: while we know that neurons can die, we lack understanding of how the death of neurons in one part of a circuit influences information processing downstream. Using the retina's well-characterized circuits, we precisely controlled the degree of cone death to understand whether partial cone loss has pathway-specific effects downstream. Visual signals transmitted from photoreceptors diverge at the dendrites of bipolar cells, the second-order neurons of the mammalian retina, into 11-15 pathways (Shekhar et al., 2016; Peng et al., 2019; Hahn et al., 2023). These secondary pathways further diverge into 17 to >30 types of ganglion cells with diverse functional properties (Chander and Chichilnisky, 2001; Kim and Rieke, 2001; Chichilnisky and Kalmar, 2002; Murphy and Rieke, 2006; Puthussery et al., 2009; Nirenberg et al., 2010; Baden et al., 2016; Grünert and Martin, 2021). In studies of injury and disease, specifically animal models of optic nerve crush, glaucoma, and retinitis pigmentosa, certain ganglion cell types tend to be more vulnerable (O'Brien et al., 2014; Ou et al., 2016; Tran et al., 2019; Wang et al., 2021; Dyszkant et al., 2025), suggesting that injury can differentially affect cell types. However, how different ganglion cell types differentially respond to common input loss remains unknown. Answering such a question has important implications for understanding how downstream neurons respond to common sensory input loss, which occurs in normal aging, neurodegeneration, and injury. Therefore, we asked how

these different pathways change upon photoreceptor loss. Previously, we demonstrated how the alpha ON-sustained (A_{ON-S}) ganglion cells, the mouse orthologue of primate ON midget ganglion cells (Hahn et al., 2023), react to partial loss of cones in the mature retina (Care et al., 2019; Lee et al., 2022). The loss of cones caused changes to the spatial receptive field of A_{ON-S} ganglion cells, including narrower centers and wider surrounds (Care et al., 2019; Lee et al., 2022). Paradoxically, this result resembles spatial receptive field changes that occur in response to increases in light levels, rather than what is expected to occur under low light levels or low signal-to-noise ratio with fewer inputs (Enroth-Cugell and Freeman, 1987; Atick and Redlich, 1990). Consistent with this interpretation, cone loss could masquerade as more light because fewer cones would release less glutamate, potentially placing the retina in a light adapted state (Man et al., 2024). If so, the signatures of light adaptation may be present across pathways. In this study, we ask if two OFF pathways exhibit global light-adapted characteristics or undergo unique pathway-specific changes after cone loss.

To answer this question, we selectively ablated cones in the adult mouse retina (Care et al., 2019; Lee et al., 2022) and examined the anatomical and functional properties across retinal pathways. We focus on two types of OFF ganglion cells: the alpha OFF-sustained (A_{OFF-S}) and alpha OFF-transient (A_{OFF-T}) ganglion cells, the mouse orthologs of primate OFF midget and OFF parasol ganglion cells, respectively (Hahn et al., 2023). A_{OFF-S} ganglion cells receive dominant inputs from type 2 (T2) and A_{OFF-T} ganglion cells are primarily driven by type 3a (T3a) OFF cone bipolar cells (Fox and Sanes, 2007; Yu et al., 2018). T2 and T3a OFF cone bipolar cells exhibit distinct temporal tuning properties (Ichinose and Hellmer, 2016) and ramify at different inner plexiform layer (IPL) depths to target A_{OFF-S} and A_{OFF-T} ganglion cells, respectively (Yu et al., 2018). Differential dynamics in these ganglion cells are thought to originate from glutamate receptors at the bipolar cell dendrites(Awatramani and Slaughter, 2000; DeVries, 2000), transmission from bipolar cells to ganglion cells, and inputs from amacrine cells (Asari and Meister, 2012; Baden et al., 2016; Franke et al., 2017).

Previous studies from direct insult to ganglion cells and photoreceptors showed differential susceptibility across ganglion cell types (Ou et al., 2016; Tran et al., 2019; Dyszkant et al., 2025), but how the circuit physiology and connectivity change before ganglion cell degeneration remains unknown. We examined whether these two OFF pathways exhibit common and/or differential responses to the loss of a shared input, aiming to understand how each pathway is impacted by damage. Specifically, can the responses to cone loss be localized to changes

before or after the divergence of these two OFF pathways? If partial cone loss induces common changes to both A_{OFF-S} and A_{OFF-T} ganglion cells, it would indicate circuitry changes before divergence of, i.e., shared inputs to, the OFF pathways (Figure 1A). Changes could occur at one or more of the following locations: cones, horizontal cells, and/or common amacrine cells. If A_{OFF-S} and A_{OFF-T} ganglion cells exhibit differential reactions to partial cone loss, it would indicate circuitry changes after divergence of, i.e., different inputs to, the OFF pathways. Changes could occur at one or more of the following locations: bipolar cells (T2 to A_{OFF-S} and T3a to A_{OFF-T}), presynaptic amacrine cells (unique ACs to T2 or T3a), and direct amacrine cells (unique ACs to A_{OFF-S} or A_{OFF-T}) (Figure 1A) (Graydon et al., 2018). We find evidence for modifications across retinal circuits, e.g., changes in excitatory and inhibitory inputs to two A_{OFF} ganglion cells, suggesting that the retina is not ubiquitously in a light-adapted state following partial cone loss. Such results are significant in demonstrating differential reactions to common input loss, their underlying mechanisms, and the potential for rescue across multiple pathways for sensory processing.

MATERIALS AND METHODS

Mice

All procedures were done in accordance with the University of California, San Francisco Institutional Animal Care and Use protocols. Animals were maintained on a 12 h dark-12 h light cycle and fed standard mouse diet ad libitum. The following transgenic mouse lines were crossed: *OPN1MWCre* (Le et al., 2004) for Cre-recombinase expression in cones expressing middle wavelength sensitive (M)-opsin, with *Rosa26-loxP-stop-loxP-DTR* (Buch et al., 2005) for Cre-dependent expression of diphtheria toxin receptor (DTR). All transgenic mice were backcrossed into the C57BL/6J background. Male and female mice were used for experiments.

Diphtheria toxin induced cone death

To induce cone death, one intramuscular diphtheria toxin injection was made between P30-40 at a dosage between 50 ng/g and 75 ng/g for OPN1MW-Cre (Care et al., 2019; Lee et al., 2022). Dosages were adjusted to induce approximately 50% cone loss. DTR-negative littermates were used as control and injected with an equivalent volume of saline. Experiments were performed within 55 days after the injection. We did not find significant changes to spatiotemporal properties across the shorter and longer halves of the interval.

Tissue preparation for immunostaining

Immunostaining protocols were identical to those described previously (Care et al., 2019; Lee et al., 2022). The retinas were fixed in 2% paraformaldehyde for 20 min at room temperature, rinsed in PBS, pH 7.42, then immersed in blocking solution (Jackson Immunoresearch, Cat# NC9624464) overnight, incubated in primary antibodies for 5 days at 4°C, then rinsed in PBS and incubated in secondary antibodies for 1 day at 4°C, and rinsed with PBS and mounted with Vectashield (Vector laboratories Cat# H-1000, RRID: AB_2336789) underneath a coverslip. The primary antibodies utilized in this study were as follows: anti-cone arrestin (Millipore Cat# AB15282, RRID:AB_1163387), anti-gephyrin (Synaptic System Cat# 147-111, RRID: AB_887719), anti-$GABA_A$Rβ2,3 (Millipore Cat# MAB341, RRID: AB_2109419), anti-GlyRα1 (Synaptic System Cat# 146111: RRID: AB_887723), anti-synaptotagmin II (Zebrafish International resource center Cat# znp-2, RRID: AB_10013783), anti-HCN4 (Alomone Labs Cat# APC-052, RRID: AB_2039906), anti-Lucifer Yellow (Life Technologies Cat# A-5750, RRID: AB_2536190), anti-CtBP2 (BD Bioscience Cat# 612044, RRID: AB_399431). Secondary antibodies used were as follows: anti-mouse-Dylight 405 (Jackson Immunoresearch Cat# 715-475-150, RRID:AB_2340839), anti-mouse-Alexa 647 (Jackson Immunoresearch Cat# 715-605-151, RRID:AB_2340863), anti-rabbit-Alexa 488 (Jackson Immunoresearch Cat# 711-545-152, RRID:AB_2313584).

Image acquisition

Type 2 and 3a OFF cone bipolar cells and their associated synaptic puncta were imaged on a Leica SP8 confocal microscope using a 40x 1.3 numerical aperture (NA) oil-immersion objective. Image stacks were acquired with a voxel size of 0.09 µm (x axis, y axis) and 0.3 µm (z axis). Each plane was acquired 2 times to obtain the average. Individual dye-filled $A_{OFF\text{-}S}$ and $A_{OFF\text{-}T}$ ganglion cells were localized using epifluorescence and their dendrites and associated synaptic puncta were imaged with the following settings: 40x (1.3 NA) objective at resolution of 0.102 x 0.102 x 0.3 µm. $A_{OFF\text{-}S}$ and $A_{OFF\text{-}T}$ ganglion cells were identified by stratification level of their dendrites (Krieger et al., 2017).

Electrophysiology tissue preparation

Procedures for patch-clamp recording of $A_{OFF\text{-}S}$ and $A_{OFF\text{-}T}$ ganglion cells in flat mount retina were identical to those described previously (Care et al., 2019, 2020; Lee et al., 2022). For bar noise stimuli (Figures 1-7), recordings were made in dorsal-nasal retina where the largest A-type ganglion cells reside (Sawant et al., 2021) and where middle (M)-wavelength sensitive opsin

dominates (Applebury et al., 2000). Following recordings, retinas were mounted on filter paper, fixed in 2% paraformaldehyde for 15-20 min, and processed for immunostaining.

Patch-clamp recordings

Patch-clamp recordings from ganglion cells were identical to those described previously (Lee et al., 2022). Patch electrodes were pulled from borosilicate glass (Sutter instruments) on a Narishige puller to 3–6 MOhm resistance. Under infrared light (950 nm), large round somas were targeted as putative $A_{OFF\text{-}S}$ ganglion cells and large oblong somas were targeted as putative $A_{OFF\text{-}T}$ ganglion cells. To type cells, extracellular spikes were recorded with an electrode filled with HEPES-buffered Ames in cell-attached configuration. $A_{OFF\text{-}S}$ ganglion cells were identified by their characteristically sustained spiking before and after a 500 ms light increment. $A_{OFF\text{-}T}$ ganglion cells were identified by their characteristically transient spiking after a 500 ms light increment. Once the the ganglion cell was identified, a new electrode was used to make an intracellular recording. Whole-cell recordings were made with an electrode filled with internal solution containing either potassium aspartate for current-clamp recordings (Figures 3I-L, 5I-N, S2F-Q, S3C-D) or cesium methane sulfonate for voltage-clamp recordings when acquired in the same cell (Figures 1I-K, 2, 3C-E, 4, 5C-H, 7, S2C-E, S3A-B) and 0.04% Lucifer yellow dye (Care et al., 2019; Lee et al., 2022). Voltage-clamp recordings were made before and after the application of 100μM picrotoxin (Thermo Fischer Scientific P1675-1G) and 5μM strychnine (Sigma-Aldrich S8753) (Figures 2, 4, 7). For perforated patch-clamp recordings in Figure S4, amphotericin-B (0.05 mg/ml) was added to the potassium aspartate internal solution in the back portion, but not the front tip, of the electrode to allow a delay before perforating the cell membrane (Care et al., 2020; Lee et al., 2022).

Light stimuli

To elicit spike responses for cell identification, a 470 nm LED was used to deliver a uniform spot 2000 μm in diameter for 500 ms using Matlab. This wavelength was used to preferentially stimulate rods between the ranges of 8–400 photoisomerizations per rod per sec (Rh*/rod/sec). Procedures for measuring the spatiotemporal receptive field profiles were identical to those described previously (Lee et al., 2022). To preferentially elicit cone-mediated responses, we presented flickering bars (width of 40μm; length of 1000μm) with intensities drawn from a Gaussian white noise distribution with mean intensity of 8,400 Rh*/rod/sec to adapt rods (Care et al., 2019; Lee et al., 2022).

Intrinsic excitability of OFF ganglion cells

For current injection experiments (Figure S4A-F), procedures were identical to those described in Lee et al. 2022 (Lee et al., 2022). Spike threshold and resting membrane potential were calculated by injecting a slow ramp of current (Figure S4G-H). Resting membrane potential was taken as the initial membrane voltage 500ms before injecting a linear current injection ramp from 0 to 300pA and spike threshold was the average voltage at which a cell initiated its first action potential in response to the ramp.

Quantification of cone numbers

Procedure for counting cones, labeled either by cone arrestin or peanut agglutinin, were identical to those described previously (Care et al., 2019; Lee et al., 2022). Briefly, images (387μm x 387μm) of cones immediately above the recorded ganglion cells were quantified in Imaris.

Quantification of synaptic density

To quantify synaptic puncta associated with specific cell types, we used confocal images of T2 and T3a OFF cone bipolar cells labeled by immunostaining for Syt2 and HCN4 in the OFF sublamina, respectively, and individual ganglion cells filled with Lucifer Yellow during physiology experiments. ImageJ (NIH RRID: SCR_003070) was used to median filter the images to remove thermal noise generated by the microscope's detectors. We created a binary mask of bipolar cell axons of interest (Amira, Thermo-Fisher Scientific RRID: SCR_014305) and VolumeCut (Della Santina et al., 2021) was used to select the OFF sublamina labeling of Syt2 and HCN4 within the IPL. Synaptic puncta associated with bipolar cell axons, $A_{OFF\text{-}S}$ and $A_{OFF\text{-}T}$ ganglion cell dendrites were identified and manually validated in ObjectFinder (Della Santina et al., 2013) with methods previously used (Lee et al., 2022). Puncta distribution of PSD95, GlyRα1, and $GABA_A$β2,3 within the dendrites of individual $A_{OFF\text{-}S}$ and $A_{OFF\text{-}T}$ ganglion cells were identified and quantified using ObjectFinder. Imaris was used to generate a 3-dimensional dendritic skeleton of the ganglion cell. Custom-written Matlab (Mathworks RRID: SCR_001622) routines were used to create a binary mask and used as a criteria to include CtBP2, GlyRα1, and $GABA_A$β2,3 that exceeds 50% overlap with a mask. Linear puncta density was calculated within a moving window of 10 μm along the dendritic skeleton, starting from the cell soma.

Linear-nonlinear model

Procedures for analyzing spatiotemporal receptive fields of spikes, subthreshold voltages, excitatory, and inhibitory currents were identical to those described previously (Lee et al., 2022). As in the previous work, we normalized the linear filter such that it was a unit vector using Igor Pro (RRID:SCR_000325). This choice of normalization places all gain information into the nonlinearity. In response to the bar stimulus, the linear filter was used to measure temporal information. A single temporal linear filter was measured by projecting the linear filters from each region of space along the first principal component measured across all filters. A single spatial filter was measured by projecting the linear filters across time along the first principal component across filters. The nonlinear component of the model maps the convolution of the linear filter and stimulus to the cell's response, i.e., spikes, voltage, excitatory current, or inhibitory current (Figures 5-7).

The linear-nonlinear model was also used in the current injection analysis (Figures S4A-F). The time-reversed spike-triggered average of the injected current represents the linear filter. The nonlinear filter is plotted with the abscissa as the convolution between the spike-triggered average and the stimulus in units of standard deviation against the ordinate, which is the spike rate (Figure S4B). The nonlinearity for each cell was interpolated and smoothed with a spline function before calculating the average.

Principal components analysis

The temporal filters (Figure 1), spatial filters (Figure 3), or the nonlinearities (Figure 5) were plotted across conditions (i.e., control, cone-DTR, and partial stimulation for $A_{OFF\text{-}S}$ and $A_{OFF\text{-}T}$ ganglion cells) in n-dimensional space, where n is the number of points in the linear filters or nonlinearities. Before running PCA, the spatial filters were aligned to their centers. We then performed pairwise comparisons of PC1 values between experimental conditions using the Wilcoxon rank-sum test. The following pairwise comparisons were tested separately for $A_{OFF\text{-}S}$ and $A_{OFF\text{-}T}$ cell types: control vs. partial, control vs. cone-DTR, and partial vs. cone-DTR.

To quantify the magnitude of change within each cell type, we computed the absolute difference in PC1 values between conditions for each cell type, and then calculated the difference between these magnitudes across cell types. For example, $|A_{OFF\text{-}T}(\text{control - partial})| - |A_{OFF\text{-}S}(\text{control - partial})|$, $|A_{OFF\text{-}T}(\text{control - cone-DTR})| - |A_{OFF\text{-}S}(\text{control - cone-DTR})|$, and $|A_{OFF\text{-}T}(\text{partial - cone-DTR}) - |A_{OFF\text{-}S}(\text{partial - cone-DTR})|$. To evaluate the significance of these differences, we bootstrapped null distributions by randomly permuting cell type identities. The resulting

distributions were centered on the observed difference of deltas. Histograms were plotted to visualize the null distributions centered at μ, with standard deviation bounds (μ±1σ and μ±2σ) to represent confidence intervals. All p-values from pairwise Wilcoxon tests and difference of delta were corrected for multiple comparisons using the Holm method.

To compare the impact on cone loss nonlinearities of inputs vs. outputs (Figure 6), nonlinearities were plotted across recording configurations for either $A_{OFF\text{-}S}$ or $A_{OFF\text{-}T}$ ganglion cells. For the pharmacological manipulations, a difference filter was calculated between the temporal (or spatial) filters and nonlinearities before and after the application of the antagonist. Average differences were for display purposes only (Figures 2, 4, 7F, I, M, P). Differences calculated for each individual cell before and after pharmacological manipulations were used for the actual analysis. For both the individual and the difference filters and nonlinearities the dimension of maximum variance was found across conditions, and that vector was assigned the first principal component (PC1). The magnitude of the projection onto the first principal component was compared between conditions: control vs. cone-DTR, control vs. partial, and cone-DTR vs. partial. The results of these comparisons were used in conjunction to assign mechanisms (Figure 1B-E).

Mean difference vector analysis

In the cases where the first principal component was found to be significantly different between control vs. cone-DTR conditions, we parameterized the filters to determine which characteristics contributed most to the observed changes (Figure S2R-T). For temporal filters, we used the following features: time to peak, time to trough, peak amplitude, trough amplitude, and time to zero crossing (Figure 1L-O). For spatial filters, we used the following features: center height, surround height, center width, and surround width (Figure 3F-H, 3L-O). Each filter, whether temporal or spatial, was represented as a point in n-dimensional space, where n is the number of observations (across space or time) within the filter. For each control filter, we then measured the extent to which modifying each feature changed the filter to become more or less like the mean cone DTR filter. This was done by linearly modifying the control filter, and then projecting that modified filter onto the n-dimensional vector that pointed from the mean control filter to the mean cone DTR filter (“mean difference vector”, representing the direction in n-dimensional space that one must travel to go from the average control filter to the average cone DTR filter; Figure S2R-T). For example, if time to peak shifted under cone loss conditions, we created a temporal filter reflecting that degree of change for each control filter, and then projected the

positions of these modified filters onto the mean difference vector. The projection values were normalized such that 1.0 corresponded to the position of the mean cone DTR filter and 0.0 corresponded to the position of the mean control filter. Thus, the closer a projection was to 1.0, the more that particular feature modification shifted the filter in the direction of cone DTR filters. This analysis was repeated for each combination of feature modifications, and the mean marginal contribution of each feature was computed across all combinations to reveal the final contribution values. Because not all features were necessarily independent, it was possible to achieve values outside the interval of [0.0, 1.0].

Quantification of movie similarity

Spatial receptive fields were generated by revolving the average linear spatial filters from control, cone-DTR and partial stimulation of control retinas. For each time point of the temporal receptive field, the corresponding spatial receptive field was calculated to form a 3D spatio-temporal receptive field. 3D convolution was applied to the movie frames using the 3D spatio-temporal receptive field to produce the filtered output movies for each condition. Such a convolution was done on 6 natural scene movies from Freiheit, 2016 (Freiheit D., 2016). The movie was converted to grayscale and segmented into multiple pieces, each lasting 5 to 10 seconds. 3D spatio-temporal receptive field sizes were scaled to convolve a reference movie across a range of resolutions: 15.42, 18.46, 160, and 640 times the receptive field pixel size. In mice, each degree of the visual field corresponds to about 31μm of the retina(Remtulla and Hallett, 1985; Schmucker and Schaeffel, 2004). Given that the receptive field sizes of alpha ganglion cells are about 300μm, which gives us 10 degrees/receptive field, and each monocular visual field spans roughly 180 degrees (Scholl et al., 2013). The mean squared error (MSE, non-perceptual similarity index) and structural similarity index (SSIM, perceptual similarity index) were used to quantify the difference between convolved movies with the reference movies as a function of movie-to-receptive field pixel ratios. MSE and SSIM across movie-to-receptive field pixel ratios are shown in Figure S6. For each frame of the movie, SSIM and MSE were calculated and the average value was reported. Procedure for analyzing static image similarity were identical to those described previously (Lee et al., 2022).

Statistical Analysis

Data are represented as median ± interquartile range (IQR) in Figures 1I-J, 2H, 2K, 2O, 2R, 3C-D, 3I-J, 4H, 4K, 4O, 4R, 5C-D, 5F-G, 5I-J, 5L-M, 7H, 7K, 7O, 7R, S2C-D, S2I-J, S2O-P, S3A, S3C, S4G-H, S5B-G, S5I-L, as mean ± sem in Figures 8C-H, and S6, and as median ±

propagated error in Figures 1K, 3E, 3K, 5E, 5H, 5K, 5N, S2E, S2K, S2Q, S3B, S3D, 6. A Wilcoxon rank-sum test (abbr. rank sum) with Holm method was used to determine significant differences across the three conditions. A permutation test with Holm method was used for Figures 1K, 3E, 3K, 5E, 5H, 5K, 5N, S2E, S2K, S2Q, S3B, S3D, 6. A two-way ANOVA test was used to determine significant differences between convolved movies [or images] with the reference movies [or images] (Figures 8 and S6). The following asterisks in the figures indicate p values: * ≤ 0.05, ** ≤ 0.01, *** ≤ 0.005.

RESULTS

Partial cone loss causes differential temporal changes to A_{OFF} ganglion cell types

To examine how retinal pathways were affected by partial cone loss, we ablated a subset of cones in mature retina by injecting diphtheria toxin (DT) into mice expressing the simian DT receptor under the M-opsin promoter at postnatal day 30 (cone-DTR) (Care et al., 2019; Lee et al., 2022). The concentration of DT was adjusted to achieve a 50-70% reduction of cones (Figure S1A-B). We examined how cone loss impacts the functional responses of OFF pathways. We targeted either A_{OFF-S} or A_{OFF-T} ganglion cells for single-cell recordings (Figure 1A). Cone-mediated inputs were elicited under three conditions: full stimulation of control retina (control), full stimulation of partial cone loss retina (cone-DTR), and partial stimulation of control retina (partial) (Figure 1B). The partial stimulation of control retina was used to determine whether changes to the spatiotemporal filter induced by partial cone loss are distinct from partial stimulation, the expectation of what would occur if the retina were purely responding as just missing a fraction of their input. For the partial stimulation, we modified a stimulus by blanking half the space to simulate unresponsive cones (Care et al., 2019; Lee et al., 2022). To determine the site of changes, we used different recording configurations to isolate inputs to and outputs from A_{OFF} ganglion cells: voltage clamp to record excitatory and inhibitory input currents and current clamp to record subthreshold voltages and output spikes (Figures 1F-G, S2). We generated a linear spatiotemporal filter for each ganglion cell type in each of the three conditions under each recording configuration (Figures 1F, S2).

First, we focus on the temporal component of the ganglion cell spatiotemporal filters (Figure 1G). There are many different aspects to the temporal filter, and we do not know, *a priori,* which, if any, might change. Therefore, we performed principal components analysis of the temporal filters under all conditions (Figures 1H, S2B, H, N) to extract the features that vary the most, and compared the strength of the projection onto the first principal component across conditions

(Figures 1I-J, S2). Given the numerous recording conditions, we present results showing significant differences between A_{OFF-S} and A_{OFF-T} ganglion cells (described below) in the main figures; the rest are in the supplementary material. To understand the mechanisms underlying changes to the temporal filter, we made pairwise comparisons of the three conditions (control vs. cone-DTR, control vs. partial stimulation, cone-DTR vs. partial stimulation) and controlled for the multiple comparisons (Figure 1B-E). For excitatory and voltage temporal filters, A_{OFF-S} ganglion cells showed differences between cone-DTR vs. partial stimulation and control vs. partial stimulation, but not between control vs. cone-DTR (Figures 1I, S2I). These results implicate compensation, i.e., a mechanism that allows responses in cone-DTR retina to match those in the full stimulation of control retina, but not match those from partial stimulation (Figure 1E). Excitatory temporal filters of A_{OFF-T} ganglion cells showed significant differences in control vs. cone-DTR and cone-DTR vs. partial, but not between control vs. partial stimulation (Figure 1J). This result implicates circuit changes, i.e., a mechanism underlying changes observed in cone-DTR that causes responses to be better or worse than control (Figure 1D); this was also found in spike temporal filters of A_{OFF-S} ganglion cells (Figure S2O). In addition to the compensation and the circuit change conclusions, described above, another possible conclusion of these types of analyses would occur if there were differences in control vs. cone-DTR and control vs. partial stimulation, but not between cone-DTR vs. partial stimulation. Such a scenario would implicate half cone stimulation as the mechanism for changes observed in cone-DTR (Figure 1C). Such mechanisms were found in inhibition from both cell types and voltage temporal filters of A_{OFF-T} ganglion cells (Figure S2C-D, J). While we emphasize the comparisons in which significant differences were detectable, some comparisons result in no evidence of differences despite cone loss or partial stimulation, which could indicate recovery from cone loss (Figure 1B). Other combinations of comparisons are interpreted as inconclusive (Figure S2A), for example, spike temporal filters of A_{OFF-T} ganglion cells (Figure S2P). Such inconclusive results could be consistent with either circuit changes or compensation; however, further studies would be required to distinguish those possibilities.

In the pairwise comparison of the three conditions for each cell type, the identification of a difference in one cell type and not the other is insufficient to conclude differential effects between the cell types (Figure 1I-J) (Nieuwenhuis et al., 2011). Therefore, to quantify the relative differences between the two ganglion cell types, we compared the magnitude of their response changes, i.e., the difference of deltas between two cell types (see Methods). First, we created a bootstrapped distribution of the null hypothesis that A_{OFF-T} and A_{OFF-S} ganglion cells

have indistinguishable changes across conditions. We then determine where the observed deltas lay relative to this distribution (Figure 1K). For two of the comparisons involving cone-DTR, i.e., (control - cone-DTR) and (partial - cone-DTR), the observed values fell in the far right tail of the null hypothesis distribution, even after controlling for the multiple comparisons, indicating that $A_{OFF\text{-}T}$ ganglion cells undergo greater changes in the excitatory temporal filter compared to $A_{OFF\text{-}S}$ ganglion cells (Figure 1K). Though we statistically compare all pairs of conditions, we highlight how much cone-DTR deviates from the control or partial stimulation conditions to isolate the effect of cone ablation. In contrast, the difference between control and partial conditions serves as a check of the analysis where we expect minimal difference if the observed delta is specifically driven by cone ablation. Temporal filters for subthreshold voltages showed greater changes in $A_{OFF\text{-}S}$ ganglion cells when we compute delta between cone-DTR vs. partial stimulation but not control vs. cone-DTR (Figure S2K). For inhibitory and spike temporal filters, we found no evidence for a difference between cell types (Figure S2E, S2Q). For the third comparison between full and partial stimulation of control retina, we consistently find no differences in the deltas across all conditions across recording configurations (Figures 1K, S2). Taken together, we find evidence that the excitatory temporal filters in the two ganglion cell types exhibited distinct mechanisms, which likely arises after the point of divergence between $A_{OFF\text{-}S}$ and $A_{OFF\text{-}T}$, i.e., at T3a cone bipolar cell inputs to $A_{OFF\text{-}T}$ ganglion cells.

We next identified which features of the temporal filter changed in the excitatory currents to explain the differences seen in both ganglion cell types (Figure 1L). Qualitatively, following partial cone loss, the $A_{OFF\text{-}S}$ temporal filter was delayed (Figure 1M), while the $A_{OFF\text{-}T}$ temporal filter lost its biphasic component (Figure 1N). To test this quantitatively, we measured the extent to which independently modifying each of five features, i.e., time to peak, time to trough, peak amplitude, trough amplitude, time to zero, made the control temporal filter more or less like the mean cone-DTR temporal filter. Briefly, this was achieved by linearly modifying each feature of individual control filters, and then measuring the projection of these modified filters along the vector that points from the mean control filter to the mean cone-DTR filter, where a value of 0 is equivalent to the mean control filter and a value of 1 is equivalent to the mean cone-DTR filter (see Methods, Figure S2R-T). For both cell types, time to peak, time to trough, peak amplitude, trough amplitude all contributed approximately 0.2 to 0.4 units normalized distance to the difference between control and cone-DTR temporal filters, while time to zero crossing contributed the most by shifting the temporal filter 0.8 units of normalized distance (Figure 1O). Taken together, we conclude that following partial cone loss the changes in excitatory temporal

filters of A_{OFF} ganglion cells reflect distinct mechanisms at post-receptoral sites, mostly captured by a delay in the time to zero crossing.

Two distinct mechanisms in inhibitory circuits underlie changes in temporal filters of A_{OFF-T} ganglion cells

To reveal the circuit mechanisms underlying the temporal changes following partial cone loss, we measured excitatory and inhibitory temporal filters of A_{OFF-S} and A_{OFF-T} ganglion cells in control and cone-DTR retina in the absence and presence of picrotoxin, an antagonist of $GABA_A$ and $GABA_C$ receptors, or strychnine, an antagonist of glycine receptors. We analyzed temporal filters to determine the contributions of GABAergic or glycinergic inhibition.

We evaluated the effect of the GABAergic (Figure 2A, D, F, M) or glycinergic (Figure 2B, E, I, P) antagonists between each control and cone-DTR condition. To this end, we subtracted the temporal filters before and after pharmacological blockade for each cell to compute a difference filter (Figure 2C). Then with the difference filters, we performed principal component analysis on the control vs. cone-DTR conditions of A_{OFF-S} and A_{OFF-T} ganglion cells (Figure 2G, J, N, Q). First, we found significant differences between the effects of glycinergic inhibition on the excitatory temporal filters of A_{OFF-T} ganglion cells under control and cone-DTR conditions (Figure 2K). Since we found above that A_{OFF-T} ganglion cells showed a difference in the changes to their excitatory temporal filters (Figure 1K), these results provide a mechanism for that difference due to diminished impact of presynaptic glycinergic inhibition on that circuit in the cone-DTR condition (Figure 2L). Second, although we found no evidence for a difference between two cell types in their inhibitory temporal filters (Figure S2E), we observed significant differences between control and cone-DTR conditions under GABAergic, but not glycinergic blockade (Figure 2O, R). These results imply that increased impact of direct GABAergic input to A_{OFF-T} ganglion cells may mask underlying differences between two cell types (Figure 2S). Taken together, these data provide evidence for two modifications to circuits of the A_{OFF-T} ganglion cell's temporal filters following partial cone loss, i.e., changes in (1) presynaptic glycinergic inhibition, consistent with changes in excitatory temporal filters (Figure 1K) and (2) direct GABAergic inhibition, which could arise from loss of cone inputs (Figure S2B-E). For the circuits of A_{OFF-S} ganglion cells, the absence of effects for blockade of glycine and GABA receptor antagonists suggests that compensation in the excitatory temporal filters is attributed to changes in direct excitatory input; however, we leave open the possibility that serial inhibition cancels the effects of each antagonist applied independently (Figure 2S).

Partial cone loss causes differential spatial changes in A_{OFF} ganglion cell types

Having observed changes to the temporal dimension of the ganglion cell responses, we next determined how partial cone loss affected spatial processing of these OFF pathways. We compared spatial filters obtained from A_{OFF-S} vs. A_{OFF-T} ganglion cells under the three conditions of control, cone-DTR, and partial stimulation, and under different recording configurations to separate input currents and output voltages and spikes (Figure 3A). We applied the same framework as described for the kinetics to determine the contributions of half cone stimulation, circuit changes, and compensation to the spatial filters of each cell type (Figure 1B-E); to compare spatial filter differences between two cell types; and to determine if these mechanisms arise prior to or after divergence between the OFF pathways.

Principal component analysis was performed on the entire spatial filter for excitation, inhibition, spikes, and subthreshold voltages (Figures 3A-B). The projection onto the first principal component of the spatial filters were significantly different between cone-DTR vs. control and cone-DTR vs. partial conditions for A_{OFF-T} excitation (Figure 3D) and voltages for both A_{OFF-S} and A_{OFF-T} voltages (Figure 3I-J), which we attribute to circuit changes. In contrast, the projection onto the first component of the A_{OFF-T} inhibitory spatial filters (Figure S3A) and A_{OFF-S} spike spatial (Figure S3C) were significantly different between cone-DTR vs. partial and control vs. partial, which we attribute to compensation. While inhibitory and spike spatial filters showed no differences between the two cell types (Figure S3B, D), we found greater spatial changes to excitatory spatial filters of A_{OFF-T} (Figure 3E) and voltage spatial filters of A_{OFF-S} ganglion cells (Figure 3K), implicating distinct circuit changes in post-receptoral circuits, i.e., cone bipolar cells, unique amacrine cell inputs, and/or intrinsic properties of ganglion cells.

Similar to the way we analyzed the temporal filters, we next determined which features of the spatial filter changed in the excitation of A_{OFF-T} ganglion cells and voltages of both A_{OFF} ganglion cells (Figure 3G, M-N) by assessing how modifying each feature of the control spatial filter better matches the cone-DTR filter. For the excitation of A_{OFF-T} ganglion cells, qualitatively, following partial cone loss, the center of the spatial filter narrowed (Figure 3G). Quantitatively, while center and surround height contribute approximately 0.1 units to the difference between control (normalized value of 0) and cone-DTR (normalized value of 1) spatial filters, center and surround widths contribute a shift of 0.4 and 0.8 units toward cone-DTR spatial filters, respectively (Figure 3H). For the voltages of both A_{OFF} ganglion cells, qualitatively, following

partial cone loss, the surround of the spatial filter widened (Figure 3M-N). Quantitatively, center and surround height and center width each contribute approximately 0.1-0.3 units to the difference between control (normalized value of 0) and cone-DTR (normalized value of 1) spatial filters (Figure 3O). While the surround width of A_{OFF-T} contributes a shift of 0.55 units toward cone-DTR spatial filters, that of A_{OFF-S} contributes 0.85 units, consistent with greater changes in A_{OFF-S} compared to A_{OFF-T} ganglion cells (Figure 3K). Taken together, we conclude that following partial cone loss, the changes in spatial filters from excitation of A_{OFF-T} and voltage of both A_{OFF} ganglion cells reflect circuit mechanisms mostly captured by a narrowing of the center and widening of the surround. These changes could arise from loss of cone inputs to bipolar cells and/or changes in presynaptic inhibition to bipolar cell inputs, and changes in amacrine cell inputs to both A_{OFF} ganglion cells independently.

Two distinct mechanisms underlie changes in spatial filters of A_{OFF-T} ganglion cells

Next, we determined the mechanisms underlying the spatial changes following partial cone loss. We measured excitatory and inhibitory spatial filters of A_{OFF-S} and A_{OFF-T} ganglion cells in control and cone-DTR retina in the absence and presence of an antagonist of $GABA_A$ and $GABA_C$ receptors (Figure 4A, D, F, M), or an antagonist of glycine receptors (Figure 4B, E, I, P). With the difference filters of the spatial filters before and after pharmacological blockade for each cell (Figure 4C), we performed principal component analysis on the control and cone-DTR conditions of A_{OFF-S} and A_{OFF-T} ganglion cells (Figure 4G, J, N, Q). First, for the A_{OFF-S} ganglion cells, we found no differences in the first principal components of the spatial filters between control vs. cone-DTR conditions under both GABAergic and glycinergic blockade (Figure 4H, K); therefore, we attributed the mechanism underlying the changes in cone-DTR in the excitatory spatial filters of A_{OFF-S} ganglion cells to excitatory circuits (Figure 4L). Second, for the A_{OFF-T} ganglion cells, we found a significant difference in the first principal components of the spatial filters between control vs. cone-DTR conditions under glycinergic blockade (Figure 4K). Since we found that A_{OFF-T} ganglion cells showed a difference in the changes to their excitatory spatial filters (Figure 3E), these results suggest that the observed difference may result from diminished presynaptic glycinergic inhibition onto bipolar cells in the cone-DTR condition (Figure 4L). Finally, similar to inhibitory temporal filters, we found no evidence for a difference between two cell types in their inhibitory spatial filters (Figure S3B). However, we observed significant differences between control and cone-DTR conditions under GABAergic, but not glycinergic blockade (Figure 4O, R). These results imply that increased impact of direct GABAergic input to A_{OFF-T} ganglion cells may mask underlying differences between two cell types (Figures 4S, S3B).

While modifications in the inhibitory spatial filters of A_{OFF-S} ganglion cells remain ambiguous without a clear mechanistic interpretation, the effects of pharmacology on the spatial filters provide evidence for three modifications to circuits of the A_{OFF} ganglion cells following partial cone loss, i.e., changes in (1) excitation to A_{OFF-S}, and (2) presynaptic glycinergic and (3) direct GABAergic inhibition to A_{OFF-T} ganglion cells.

Partial cone loss affects nonlinearities at multiple levels leading to partial recovery of A_{OFF} ganglion cell outputs

The linear spatiotemporal filters described above map onto the cell's actual response with a nonlinearity, which reflects average changes in response magnitude to a given change in stimulus contrast. For both cell types, cone-DTR shows shallower input nonlinearities, compared to control, that become steeper in output voltages and spikes (Figure 5A). To quantify this input-to-output transformation, we performed principal component analysis on the entire nonlinearity, where more negative PC1 corresponds to a shallower nonlinearity (Figure 5B). Indeed, we found that cone-DTR exhibited decreased excitatory input currents to A_{OFF-S} and A_{OFF-T}, and inhibitory input currents to A_{OFF-T} ganglion cells compared to both full and partial stimulation of control conditions (Figure 5C-D and G). Therefore, we attribute the mechanism to circuit changes, which arise from bipolar and amacrine cells. For the subthreshold voltage nonlinearities, the A_{OFF-S} ganglion cells had no significant differences in the cone-DTR vs. control, i.e., no change (Figure 5I). In contrast, A_{OFF-T} ganglion cells showed significantly shallower voltage nonlinearities in cone-DTR compared to control (Figure 5J). This demonstrates that the nonlinearity does not fully recover to control values, consistent with greater changes observed in A_{OFF-T} ganglion cells in cone-DTR retina (Figure 5K). Interestingly, although the mechanism of voltages of A_{OFF-T} remains inconclusive (Figure 5J), spike nonlinearities in the cone-DTR condition were significantly different from both control and partial stimulation, i.e., with a mechanistic interpretation of circuit changes (Figure 5M). This results in greater changes to A_{OFF-T} compared to A_{OFF-S} ganglion cells (Figure 5N). Unlike the reduced inputs, the PC1 of spike nonlinearities in A_{OFF-T} ganglion cells of cone-DTR shifted toward positive PC1 values, i.e., steeper nonlinearity, demonstrating recovery of the voltage-to-spike transformation (Figure 5M).

Having found these differences between input and output nonlinearities, we next evaluated whether cone loss differentially affects nonlinearities of inputs vs. outputs across conditions. In

both cell types, cone loss consistently resulted in greater changes in input currents than in output voltages or spikes (Figure 6B, D, F, H) in the comparisons between control vs. cone-DTR and partial vs. cone-DTR. To verify the quantification method, the comparisons between control vs. partial showed no significant differences between input currents and output voltages and spikes as expected.

Given that the spike nonlinearities of cone-DTR were different from control (Figure 5M), we asked whether cone loss induced changes in intrinsic excitability of A_{OFF-T} ganglion cells. We tested this by measuring spikes in response to injected white noise currents into A_{OFF} ganglion cells under perforated patch-clamp configuration (Chichilnisky and Kalmar, 2002; Care et al., 2019; Lee et al., 2022). We found no evidence to support this possibility for both A_{OFF-S} and A_{OFF-T} ganglion cells (Figure S4A-F). However, changes in intrinsic properties, such as resting membrane potential and spike threshold, could be missed as the membrane potentials were artificially held at -60mV. Therefore, we injected a slow ramp of current to induce spikes to capture intrinsic differences between these two cell types. This revealed that cone loss depolarized the resting membrane potential of A_{OFF-T} ganglion cells with a maintained spike threshold (Figure S4G-H), which could account for a steeper voltage-to-spike transformation (Figure 5A). Although the effect of cone-DTR resulted in inconclusive mechanisms in inhibitory currents from A_{OFF-S} ganglion cells, shallower nonlinearities of input currents in both cell types suggest common effects of cone loss on two OFF pathways. This was further supported by the greater effect of cone-DTR onto input currents than outputs. Furthermore, nonlinearity differences between subthreshold voltages and spikes arise from intrinsic differences in A_{OFF-T} ganglion cells, suggesting that in addition to cone loss affecting cone bipolar and amacrine cells, cone loss evoked changes at the level of the ganglion cells.

Three distinct mechanisms underlie changes in nonlinearities of both A_{OFF-S} and A_{OFF-T} ganglion cells upon partial cone loss

Having found circuit changes to excitatory and inhibitory nonlinearities following partial cone loss (Figures 5 and 6), we evaluated the differences between the input current nonlinearities before and after GABAergic or glycinergic antagonists (Figure 7A-E) to determine the underlying mechanisms. The first principal components of the excitatory nonlinearity differences were not significantly different between control vs. cone-DTR conditions for both GABAergic and glycinergic blockade, suggesting changes in excitatory circuits to A_{OFF-S} and A_{OFF-T} ganglion cells of cone-DTR retina (Figure 7F-L). On the other hand, we found the first principal components of

inhibitory nonlinearity differences from both ganglion cell types were significantly different between control vs. cone-DTR conditions under GABAergic blockade (Figure 7O), suggesting an increased impact of direct GABAergic inhibition onto A_{OFF-S} and A_{OFF-T} ganglion cells (Figure 7S). In addition, the first principal components of the inhibitory nonlinearity differences in A_{OFF-T} ganglion cells from cone-DTR had an increased impact of glycinergic blockade from that of control retina (Figure 7R). Therefore, we attributed the mechanism underlying changes to the nonlinearity of A_{OFF-T} ganglion cells to both direct GABAergic and glycinergic inhibition (Figure 7S). Having found functional evidence for glutamatergic, GABAergic, and glycinergic modifications following partial cone loss, we also examined synaptic puncta in the bipolar and ganglion cells of these two retinal pathways. We found a subset of the anatomical parameters correlated with functional findings (Figure S5). Specifically, we found increased size of excitatory synapses at T2 and T3a bipolar cells and increased density of $GABA_A$ receptors at T3a bipolar cells. Also we found increased size of $GABA_A$ receptors at both A_{OFF} ganglion cell types.

Taken together, these data provide evidence for common modifications of excitatory circuits following partial cone loss in A_{OFF-S} and A_{OFF-T} ganglion cells. Additionally, inhibitory circuits undergo two distinct modifications: (1) direct GABAergic inhibition onto A_{OFF-S} ganglion cells, and (2) direct GABAergic and glycinergic inhibition onto A_{OFF-T} ganglion cells.

Following partial cone loss, spatiotemporal modifications have minimal consequences on the perception of natural movies

These ganglion cell spatiotemporal filters ultimately serve vision; therefore, we determined how the observed ganglion cell spatiotemporal modifications could contribute to preserve perceptually relevant information by using the measured spatiotemporal filters of subthreshold voltages applied to natural scenes. To quantify movies filtered by the receptive fields of (1) full stimulation of control retina, (2) cone-DTR retina, and (3) partial stimulation of control retina, we used two metrics to quantify the similarity between filtered and original movies: (a) the inverse of a mean squared error (MSE), which we call a non-perceptual similarity index, and (b) a perceptually relevant structural similarity index (SSIM) modeled off the human visual system, which evaluates three features of an image: luminance, contrast, and structure (Wang et al., 2004; Lee et al., 2022; Gogliettino et al., 2023). We previously showed that static natural images filtered by A_{ON-S} ganglion cell spatial receptive fields following partial cone loss were indistinguishable from those filtered by control A_{ON-S} ganglion cell spatial receptive fields when evaluated by the SSIM, the perceptual similarity index, but were significantly worse when

evaluated by the non-perceptual similarity metric (Lee et al., 2022). To address whether spatial and temporal filters from individual pathways show differences in the filtered movies, we included A_{ON-S} ganglion cells in our comparison with both types of A_{OFF} ganglion cells (Figure 8). Now applied to natural movies, the non-perceptual image similarity, as quantified by 1/MSE, showed differences across conditions and cell types. When we compared across conditions within each cell type, we found that movies filtered by cone-DTR receptive fields of A_{ON-S} and A_{OFF-T} ganglion cells were significantly different from movies filtered by the control filters, while those filtered by A_{OFF-S} ganglion cells were not significantly different in non-perceptual similarity (Figure 8C-E). However, such differences in A_{OFF-T} ganglion cells were not found when evaluated by SSIM (Figure 8H). In contrast, A_{ON-S} ganglion cells of cone-DTR retina showed lower SSIM compared to that of control (Figure 8F). When we compare between OFF cells, movies filtered by A_{OFF-T} ganglion cells in cone-DTR retina, which showed lower similarity in the rudimentary comparison of mean squared error, were perceptually indistinguishable from movies filtered by A_{OFF-T} ganglion cells in control retina (Figure 8G-H). In addition, we found differences across cell types. As expected, movies filtered by receptive fields of A_{ON-S} ganglion cells in all three conditions had greater similarity due to preserved polarity in both metrics (Figure S6A-F). Between the two OFF ganglion cell types, similarity quantified by 1/MSE was comparable in cone-DTR (Figure S6B), however, A_{OFF-T} ganglion cells showed higher perceptual similarity to the original movies compared to A_{OFF-S} ganglion cells (Figure S6E). Together, our results demonstrate heterogeneity between ON and OFF pathways in filtering natural movies as well as differences between two A_{OFF} ganglion cells, i.e., changes in spatiotemporal properties of A_{OFF-T} ganglion cells shapes their output to more effectively preserve perceptually relevant features of natural movies compared to A_{OFF-S} ganglion cells. These results suggest that spatial and temporal changes observed in A_{OFF-T} ganglion cells following partial cone loss contribute to preserving perceptually relevant features of natural movies.

DISCUSSION

Results demonstrate that both A_{OFF-S} and A_{OFF-T} ganglion cells undergo different temporal and spatial modifications in response to partial cone loss that cannot be recapitulated by partial stimulation of control mature retina, providing evidence for retinal circuit changes unique to each pathway. We compared differences in temporal and spatial properties across cone stimulation and cone loss conditions and categorized mechanisms for changes in cone-DTR retina. We found that A_{OFF-S} ganglion cells undergo compensatory changes and A_{OFF-T} ganglion cells undergo circuit changes which lead to differences in their linear temporal filters (Figure 1).

Pharmacological manipulations revealed changes to excitatory circuits of A_{OFF-S} ganglion cells, and in inhibitory circuits of A_{OFF-T} ganglion cells, i.e., presynaptic glycinergic inhibition and direct GABAergic inhibition (Figure 2). We also found that changes in excitatory and inhibitory spatial filters arise from glycinergic presynaptic inhibition and direct GABAergic inhibition onto A_{OFF-T} ganglion cells (Figures 3-4). Lastly, unlike input nonlinearities, we found recovery of the voltage-to-spike transformation in A_{OFF-T} ganglion cells, which involves changes in intrinsic properties (Figures 5, S4G). Pharmacological manipulations revealed mechanistic changes to A_{OFF-S} and A_{OFF-T} ganglion cells, i.e., excitation and direct GABAergic and glycinergic inhibition (Figure 7), suggesting that cone loss affects nonlinearities at multiple levels that ultimately lead to partial recovery of A_{OFF-T} ganglion cell outputs. While A_{OFF-S} ganglion cells receive direct inhibitory inputs from AII amacrine cells (Manookin et al., 2008; van Wyk et al., 2009), we did not detect changes in glycinergic inhibition in A_{OFF-S} cells across conditions. In contrast, we found changes in both glycinergic and GABAergic inhibition onto A_{OFF-T} ganglion cells indicating modifications of multiple inhibitory pathways, potentially including AII amacrine cells. Each of these results support the conclusions that neither partial light stimulation alone nor light adaptation are sufficient to elicit the changes following partial cone loss. Finally, the accumulation of evidence that A_{OFF-T} ganglion cells exhibit more circuitry changes following partial cone loss resulted in a greater preservation of perceptually relevant features in natural movies filtered by cone-DTR receptive fields (Figure 8). Our study finds multiple sites of modifications in the retinal circuit after divergence of the two OFF pathways, indicating functional differences in response to common input loss. Such distinct circuit changes, in turn, contribute to preserving perceptually relevant information.

Previously, we showed that partial cone loss triggers changes in inhibitory circuits in the ON pathway, specifically in pathways leading to the A_{ON-S} ganglion cells. A_{ON-S} ganglion cells exhibited expansion of receptive field surrounds, greater temporal integration, recovery of inhibitory gain and enhancement of inhibitory synapses in the dendrites. We determined that inhibition compensates for fewer cones to preserve perception of static natural images (Lee et al., 2022). Both ON and OFF pathways exhibited some common spatial changes following partial cone loss, i.e., surround expansion. Yet, we found a difference in adjusting kinetics across retinal pathways after cone loss (Lee et al., 2022) (Figure 1) consistent with previous studies in control retina (Chander and Chichilnisky, 2001; Kim and Rieke, 2001). Specifically, cone-DTR retina of A_{OFF-T} ganglion cells exhibited greater degree of changes in excitatory temporal filters compared to that of A_{OFF-S} ganglion cells. We speculate that while spatial

changes were sufficient to maintain the quality of static images across cell types (Lee et al., 2022) (Figure S6I-L), temporal changes in A_{OFF-T} ganglion cells contribute to achieve higher perceptual similarity in filtering movies (Figure 8). Expansion of the surround and loss of the biphasic component could be attributed to potential changes in inhibition, for example, changes in inhibitory inputs onto A_{OFF-T} ganglion cells (Figures 2, 4, 7 and S5). At the same time, we found that changes in excitatory circuits are a common consequence of global disruption of cones. Future experiments assessing the potential upregulation of developmentally-expressed receptor subunits following cone loss will determine the contributions of GABAergic and glycinergic amacrine cells in shaping visual outputs (Sinha et al., 2021). A_{OFF-T} ganglion cells tend to be more vulnerable among the mouse ganglion cell types in other manipulations of the retinal circuit, e.g., models of glaucoma and optic nerve crush (Ou et al., 2016; Tran et al., 2019). Perhaps differences in manipulation cause differential responses across ganglion cell types and/or perhaps the plasticity of inhibitory circuits leading to the A_{OFF-T} ganglion cells render them robust in some conditions or up to certain thresholds of damage and then render them particularly vulnerable beyond those thresholds. Future work comparing how retinal circuits react across manipulations could distinguish among these possibilities. Finally, considering the transcriptional similarity between A_{OFF-T} and A_{OFF-S} ganglion cell types (Tran et al., 2019), differences in vulnerability of these two cell types across manipulations could be attributed to intrinsic properties not discernible by their transcriptomic profiles and/or by their extrinsic properties, i.e., circuit inputs.

Spatial and temporal adjustments following input loss found in cone-DTR retina demonstrate how functional homeostasis restores neuronal activity to a set point following perturbation. Homeostatic plasticity in the retina has been observed broadly: (1) potentiation of rod-to-rod bipolar cells in the rod degeneration *P23H* mice to maintain light sensitivity (Leinonen et al., 2020), (2) structural and functional compensation at second-order synapses upon partial loss of photoreceptors (Care et al., 2019, 2020; Shen et al., 2020; Lee et al., 2022), (3) preserved cone-mediated light responses and fidelity of information transmission in a *CNGB1* model of rod degeneration(Scalabrino et al., 2022), (4) maintained light responses in cones lacking outer segments in the rod degeneration *rd10* mouse (Xu et al., 2022; Ellis et al., 2023), and (5) retained signal transmission and processing capacity of surviving circuitry in the rod degeneration *rd1* mouse (Rodgers et al., 2023). Despite differences in the etiologies of photoreceptor death, these studies provide evidence that post-receptoral circuits can retain function during degeneration, which is consistent with our findings on functional adjustments

that preserve perceptually relevant information within natural movies (Figure 8). The present observation of changes in temporal filters following partial cone loss emphasizes that such changes would be missed by conventional diagnostic tools for acuity which tend not to limit decision time for letter identification (Ferris et al., 1982; Ratnam et al., 2013; Foote et al., 2018). Such resiliency within the retina inspires efforts to develop (1) diagnostics sensitive to mild changes and (2) strategies to preserve surviving circuits to restore visual function. For example, computational models of morphologically accurate healthy and degenerated retina revealed maintained responsiveness of ON and OFF cone bipolar cells to electrical stimulation in degenerated retina (Farzad et al., 2023). Based on the resilience of cone vision, cone preservation would be a promising therapeutic strategy. However, further studies are required to determine the time window for effective intervention as a circuit's rewiring capacity, cone-mediated light responses, and visual behaviors all decline with age (Shen et al., 2020).

While our original findings suggested that the effects of partial cone loss could be interpreted as the entire retina sitting in a light adapted state (Lee et al., 2021), the present study demonstrates that retinal pathways undergo distinct functional and structural modifications. Maintenance of general center-surround receptive field structures and the fidelity of signaling despite input loss demonstrate compensatory changes that minimally degrade function. Such adaptive changes following input loss have been observed across sensory circuits. For example, in the auditory system, reduced input following noise-induced damage to the synapses of hair cells in the inner ear (cochlear synaptopathy) led to an increase in neural gain across a wide range of frequencies to compensate for input loss (Barbour, 2020; Monaghan et al., 2020). Similarly, acoustic trauma caused auditory cortical neurons to exhibit increased tone-evoked responses as a result of dynamic properties of inhibition, which led to the expansion of receptive fields(Scholl and Wehr, 2008). Another study reported the recovery of functional patterns of auditory cortical activity potentially via changes in the balance of excitatory and inhibitory inputs in adult-onset deafness (Karoui et al., 2023). Across the auditory and visual systems, inhibitory neurons exhibit greater dynamics than excitatory neurons (Villa et al., 2016; Eavri et al., 2018). For example, in the visual system, greater flexibility of inhibitory circuits were found both in the visual cortex and in the retina as reported here (Lee et al., 2022). Even beyond pathways within one sensory system, robust plasticity in the form of cortical reorganization has been observed in compensation across sensory modalities in the mature nervous system (Jitsuki et al., 2011; Petrus et al., 2014; Ewall et al., 2021; Kral and Sharma, 2023).

Previous studies have shown that neurons exhibit different vulnerability and plasticity upon deafferentation (O'Brien et al., 2014; Ou et al., 2016; Villa et al., 2016; Eavri et al., 2018; Tran et al., 2019; Wang et al., 2021; Karoui et al., 2023; Kumar et al., 2023; Dyszkant et al., 2025), but how each cell type responds and where these changes occur within the circuits have not been examined. By investigating spatiotemporal properties of two different types of A_{OFF} ganglion cells, we demonstrate unique outcomes in response to common input loss and provide mechanistic insights on those changes across recording configuration through pharmacology. Moreover, we assessed the consequences of changes in spatiotemporal processing on visual perception of natural movies, which incorporates a dimension beyond previous assessments of static natural scenes.

CONFLICT OF INTEREST: The authors declare no competing interests.

ACKNOWLEDGEMENT: We thank Annika Balraj, Jonah Chan, Jeanette Hyer, Yvonne Ou, Fred Rieke, Rachel O.L. Wong for helpful discussions and comments. This work was supported by NIH through the Vision Core Grants P30 EY002162 (UCSF), K99EY033858 (J.Y.L) and EY029772 (F.A.D.) and by foundation grants from McKnight Scholar Award, Research to Prevent Blindness Unrestricted Grant, and All May See.

AUTHOR CONTRIBUTION

Conceptualization, methodology, software, resources, writing – review & editing, J.Y.L., D.B.K, S.C.H, and F.A.D.; formal analysis, J.Y.L., D.B,K, S.C.B, L.D.S., J.V.J., and F.A.D.; investigation, visualization, J.Y.L. and F.A.D.; data curation; J.Y.L., D.B,K.; validation, writing – original draft, supervision, project administration, funding acquisition, J.Y.L. and F.A.D.

DATA AVAILABILITY

- All data reported in this paper will be shared by the lead contacts upon request.
- Any additional information required to reanalyze the data reported in this paper is available from the lead contact upon request.

CODE ACCESSIBILITY

- All original code for the image analysis has been deposited at Github and is publically available as of the date of publication. The information is listed in the key resources table.

SUPPLEMENTAL MATERIAL

Figures S1-S6 and Dataset S1.

REFERENCES

Applebury ML, Antoch MP, Baxter LC, Chun LL, Falk JD, Farhangfar F, Kage K, Krzystolik MG, Lyass LA, Robbins JT (2000) The murine cone photoreceptor: a single cone type expresses both S and M opsins with retinal spatial patterning. Neuron 27:513–523.

Asari H, Meister M (2012) Divergence of visual channels in the inner retina. Nat Neurosci 15:1581–1589.

Atick JJ, Redlich AN (1990) Towards a Theory of Early Visual Processing. Neural Comput 2:308–320.

Awatramani GB, Slaughter MM (2000) Origin of transient and sustained responses in ganglion cells of the retina. J Neurosci Off J Soc Neurosci 20:7087–7095.

Baden T, Berens P, Franke K, Román Rosón M, Bethge M, Euler T (2016) The functional diversity of retinal ganglion cells in the mouse. Nature 529:345–350.

Barbour DL (2020) Hidden Hearing Loss: Mixed Effects of Compensatory Plasticity. Curr Biol 30:R1433–R1436.

Buch T, Heppner FL, Tertilt C, Heinen TJAJ, Kremer M, Wunderlich FT, Jung S, Waisman A (2005) A Cre-inducible diphtheria toxin receptor mediates cell lineage ablation after toxin administration. Nat Methods 2:419–426.

Care RA, Anastassov IA, Kastner DB, Kuo Y-M, Della Santina L, Dunn FA (2020) Mature Retina Compensates Functionally for Partial Loss of Rod Photoreceptors. Cell Rep 31:107730.

Care RA, Kastner DB, De la Huerta I, Pan S, Khoche A, Della Santina L, Gamlin C, Santo Tomas C, Ngo J, Chen A, Kuo Y-M, Ou Y, Dunn FA (2019) Partial Cone Loss Triggers Synapse-Specific Remodeling and Spatial Receptive Field Rearrangements in a Mature Retinal Circuit. Cell Rep 27:2171-2183.e5.

Chander D, Chichilnisky EJ (2001) Adaptation to temporal contrast in primate and salamander

retina. J Neurosci Off J Soc Neurosci 21:9904–9916.

Chichilnisky EJ, Kalmar RS (2002) Functional Asymmetries in ON and OFF Ganglion Cells of Primate Retina. J Neurosci 22:2737–2747.

Della Santina L, Inman DM, Lupien CB, Horner PJ, Wong ROL (2013) Differential progression of structural and functional alterations in distinct retinal ganglion cell types in a mouse model of glaucoma. J Neurosci Off J Soc Neurosci 33:17444–17457.

Della Santina L, Yu AK, Harris SC, Soliño M, Garcia Ruiz T, Most J, Kuo Y-M, Dunn FA, Ou Y (2021) Disassembly and rewiring of a mature converging excitatory circuit following injury. Cell Rep 36:109463.

DeVries SH (2000) Bipolar Cells Use Kainate and AMPA Receptors to Filter Visual Information into Separate Channels. Neuron 28:847–856.

Dyszkant N, Oesterle J, Qiu Y, Harrer M, Schubert T, Gonschorek D, Euler T (2025) Photoreceptor degeneration has heterogeneous effects on functional retinal ganglion cell types. J Physiol.

Eavri R, Shepherd J, Welsh CA, Flanders GH, Bear MF, Nedivi E (2018) Interneuron Simplification and Loss of Structural Plasticity As Markers of Aging-Related Functional Decline. J Neurosci 38:8421–8432.

Ellis EM, Paniagua AE, Scalabrino ML, Thapa M, Rathinavelu J, Jiao Y, Williams DS, Field GD, Fain GL, Sampath AP (2023) Cones and cone pathways remain functional in advanced retinal degeneration. Curr Biol CB 33:1513-1522.e4.

Enroth-Cugell C, Freeman AW (1987) The receptive-field spatial structure of cat retinal Y cells. J Physiol 384:49–79.

Ewall G, Parkins S, Lin A, Jaoui Y, Lee H-K (2021) Cortical and Subcortical Circuits for Cross-Modal Plasticity Induced by Loss of Vision. Front Neural Circuits 15:665009.

Farzad S, Kosta P, Iseri E, Walston ST, Bouteiller J-MC, Pfeiffer RL, Sigulinsky CL, Yang J-H, Garcia JC, Anderson JR, Jones BW, Lazzi G (2023) Impact of Retinal Degeneration on Response of ON and OFF Cone Bipolar Cells to Electrical Stimulation. IEEE Trans Neural Syst Rehabil Eng Publ IEEE Eng Med Biol Soc 31:2424–2437.

Ferris FL, Kassoff A, Bresnick GH, Bailey I (1982) New visual acuity charts for clinical research. Am J Ophthalmol 94:91–96.

Foote KG, Loumou P, Griffin S, Qin J, Ratnam K, Porco TC, Roorda A, Duncan JL (2018) Relationship Between Foveal Cone Structure and Visual Acuity Measured With Adaptive Optics Scanning Laser Ophthalmoscopy in Retinal Degeneration. Invest Ophthalmol Vis Sci 59:3385–3393.

Fox MA, Sanes JR (2007) Synaptotagmin I and II are present in distinct subsets of central synapses. J Comp Neurol 503:280–296.

Franke K, Berens P, Schubert T, Bethge M, Euler T, Baden T (2017) Inhibition decorrelates visual feature representations in the inner retina. Nature 542:439–444.

Freiheit D. (2016) GoPro Awards: Squirrel Runs Off With GoPro.

Gogliettino AR, Madugula SS, Grosberg LE, Vilkhu RS, Brown J, Nguyen H, Kling A, Hottowy P, Dąbrowski W, Sher A, Litke AM, Chichilnisky EJ (2023) High-Fidelity Reproduction of Visual Signals by Electrical Stimulation in the Central Primate Retina. J Neurosci 43:4625–4641.

Graydon CW, Lieberman EE, Rho N, Briggman KL, Singer JH, Diamond JS (2018) Synaptic Transfer between Rod and Cone Pathways Mediated by AII Amacrine Cells in the Mouse Retina. Curr Biol CB 28:2739-2751.e3.

Grünert U, Martin PR (2021) Morphology, Molecular Characterization, and Connections of Ganglion Cells in Primate Retina. Annu Rev Vis Sci 7:73–103.

Hahn J, Monavarfeshani A, Qiao M, Kao AH, Kölsch Y, Kumar A, Kunze VP, Rasys AM, Richardson R, Wekselblatt JB, Baier H, Lucas RJ, Li W, Meister M, Trachtenberg JT, Yan W, Peng Y-R, Sanes JR, Shekhar K (2023) Evolution of neuronal cell classes and types in the vertebrate retina. Nature 624:415–424.

Ichinose T, Hellmer CB (2016) Differential signalling and glutamate receptor compositions in the OFF bipolar cell types in the mouse retina. J Physiol 594:883–894.

Jitsuki S, Takemoto K, Kawasaki T, Tada H, Takahashi A, Becamel C, Sano A, Yuzaki M, Zukin RS, Ziff EB, Kessels HW, Takahashi T (2011) Serotonin mediates cross-modal

reorganization of cortical circuits. Neuron 69:780–792.

Karoui C, Strelnikov K, Payoux P, Salabert A-S, James CJ, Deguine O, Barone P, Marx M (2023) Auditory cortical plasticity after cochlear implantation in asymmetric hearing loss is related to spatial hearing: a PET H215O study. Cereb Cortex 33:2229–2244.

Kim KJ, Rieke F (2001) Temporal Contrast Adaptation in the Input and Output Signals of Salamander Retinal Ganglion Cells. J Neurosci 21:287–299.

Kral A, Sharma A (2023) Crossmodal plasticity in hearing loss. Trends Neurosci 46:377–393.

Krieger B, Qiao M, Rousso DL, Sanes JR, Meister M (2017) Four alpha ganglion cell types in mouse retina: Function, structure, and molecular signatures. PloS One 12:e0180091.

Kumar M, Handy G, Kouvaros S, Zhao Y, Brinson LL, Wei E, Bizup B, Doiron B, Tzounopoulos T (2023) Cell-type-specific plasticity of inhibitory interneurons in the rehabilitation of auditory cortex after peripheral damage. Nat Commun 14:4170.

Le Y-Z, Ash JD, Al-Ubaidi MR, Chen Y, Ma J-X, Anderson RE (2004) Targeted expression of Cre recombinase to cone photoreceptors in transgenic mice. Mol Vis 10:1011–1018.

Lee JY, Care RA, Della Santina L, Dunn FA (2021) Impact of Photoreceptor Loss on Retinal Circuitry. Annu Rev Vis Sci 7:105–128.

Lee JY, Care RA, Kastner DB, Della Santina L, Dunn FA (2022) Inhibition, but not excitation, recovers from partial cone loss with greater spatiotemporal integration, synapse density, and frequency. Cell Rep 38:110317.

Leinonen H, Pham NC, Boyd T, Santoso J, Palczewski K, Vinberg F (2020) Homeostatic plasticity in the retina is associated with maintenance of night vision during retinal degenerative disease. eLife 9:e59422.

Liu Y, Gao Z, Chen C, Wen B, Huang L, Ge R, Zhao S, Fan R, Feng J, Lu W, Wang L, Wang J-H (2017) Piriform cortical glutamatergic and GABAergic neurons express coordinated plasticity for whisker-induced odor recall. Oncotarget 8:95719–95740.

Man L, Ganzen L, Nawy S, Thoreson WB, Kramer R (2024) Knockout of Calcium-Dependent Neurotransmitter Release from Rods and Cones Triggers Downstream Retinal

Remodeling. Invest Ophthalmol Vis Sci 65:4449–4449.

Manookin MB, Beaudoin DL, Ernst ZR, Flagel LJ, Demb JB (2008) Disinhibition Combines with Excitation to Extend the Operating Range of the OFF Visual Pathway in Daylight. J Neurosci 28:4136–4150.

Monaghan JJM, Garcia-Lazaro JA, McAlpine D, Schaette R (2020) Hidden Hearing Loss Impacts the Neural Representation of Speech in Background Noise. Curr Biol 30:4710-4721.e4.

Murphy GJ, Rieke F (2006) Network Variability Limits Stimulus-Evoked Spike Timing Precision in Retinal Ganglion Cells. Neuron 52:511–524.

Nieuwenhuis S, Forstmann BU, Wagenmakers E-J (2011) Erroneous analyses of interactions in neuroscience: a problem of significance. Nat Neurosci 14:1105–1107.

Nirenberg S, Bomash I, Pillow JW, Victor JD (2010) Heterogeneous response dynamics in retinal ganglion cells: the interplay of predictive coding and adaptation. J Neurophysiol 103:3184–3194.

O'Brien EE, Greferath U, Fletcher EL (2014) The effect of photoreceptor degeneration on ganglion cell morphology: Ganglion cells in retinal degeneration. J Comp Neurol 522:1155–1170.

Ou Y, Jo RE, Ullian EM, Wong ROL, Della Santina L (2016) Selective Vulnerability of Specific Retinal Ganglion Cell Types and Synapses after Transient Ocular Hypertension. J Neurosci Off J Soc Neurosci 36:9240–9252.

Peng Y-R, Shekhar K, Yan W, Herrmann D, Sappington A, Bryman GS, van Zyl T, Do MTH, Regev A, Sanes JR (2019) Molecular Classification and Comparative Taxonomics of Foveal and Peripheral Cells in Primate Retina. Cell 176:1222-1237.e22.

Petrus E, Isaiah A, Jones AP, Li D, Wang H, Lee H-K, Kanold PO (2014) Crossmodal induction of thalamocortical potentiation leads to enhanced information processing in the auditory cortex. Neuron 81:664–673.

Puthussery T, Gayet-Primo J, Pandey S, Duvoisin RM, Taylor WR (2009) Differential loss and preservation of glutamate receptor function in bipolar cells in the rd10 mouse model of

retinitis pigmentosa. Eur J Neurosci 29:1533–1542.

Ratnam K, Carroll J, Porco TC, Duncan JL, Roorda A (2013) Relationship Between Foveal Cone Structure and Clinical Measures of Visual Function in Patients With Inherited Retinal Degenerations. Investig Opthalmology Vis Sci 54:5836.

Remtulla S, Hallett PE (1985) A schematic eye for the mouse, and comparisons with the rat. Vision Res 25:21–31.

Rodgers J, Hughes S, Lindner M, Allen AE, Ebrahimi AS, Storchi R, Peirson SN, Lucas RJ, Hankins MW (2023) Functional integrity of visual coding following advanced photoreceptor degeneration. Curr Biol CB 33:474-486.e5.

Sawant A, Ebbinghaus BN, Bleckert A, Gamlin C, Yu W-Q, Berson D, Rudolph U, Sinha R, Hoon M (2021) Organization and emergence of a mixed GABA-glycine retinal circuit that provides inhibition to mouse ON-sustained alpha retinal ganglion cells. Cell Rep 34:108858.

Scalabrino ML, Thapa M, Chew LA, Zhang E, Xu J, Sampath AP, Chen J, Field GD (2022) Robust cone-mediated signaling persists late into rod photoreceptor degeneration. eLife 11:e80271.

Schmucker C, Schaeffel F (2004) A paraxial schematic eye model for the growing C57BL/6 mouse. Vision Res 44:1857–1867.

Scholl B, Burge J, Priebe NJ (2013) Binocular integration and disparity selectivity in mouse primary visual cortex. J Neurophysiol 109:3013–3024.

Scholl B, Wehr M (2008) Disruption of Balanced Cortical Excitation and Inhibition by Acoustic Trauma. J Neurophysiol 100:646–656.

Shekhar K, Lapan SW, Whitney IE, Tran NM, Macosko EZ, Kowalczyk M, Adiconis X, Levin JZ, Nemesh J, Goldman M, McCarroll SA, Cepko CL, Regev A, Sanes JR (2016) Comprehensive Classification of Retinal Bipolar Neurons by Single-Cell Transcriptomics. Cell 166:1308-1323.e30.

Shen N, Wang B, Soto F, Kerschensteiner D (2020) Homeostatic Plasticity Shapes the Retinal Response to Photoreceptor Degeneration. Curr Biol 30:1916-1926.e3.

Sinha R, Grimes WN, Wallin J, Ebbinghaus BN, Luu K, Cherry T, Rieke F, Rudolph U, Wong RO, Hoon M (2021) Transient expression of a GABA receptor subunit during early development is critical for inhibitory synapse maturation and function. Curr Biol 31:4314-4326.e5.

Tran NM, Shekhar K, Whitney IE, Jacobi A, Benhar I, Hong G, Yan W, Adiconis X, Arnold ME, Lee JM, Levin JZ, Lin D, Wang C, Lieber CM, Regev A, He Z, Sanes JR (2019) Single-Cell Profiles of Retinal Ganglion Cells Differing in Resilience to Injury Reveal Neuroprotective Genes. Neuron 104:1039-1055.e12.

van Wyk M, Wässle H, Taylor WR (2009) Receptive field properties of ON- and OFF-ganglion cells in the mouse retina. Vis Neurosci 26:297–308.

Villa KL, Berry KP, Subramanian J, Cha JW, Oh WC, Kwon H-B, Kubota Y, So PTC, Nedivi E (2016) Inhibitory Synapses Are Repeatedly Assembled and Removed at Persistent Sites In Vivo. Neuron 89:756–769.

Wang AYM, Wong VHY, Lee PY, Bui BV, Dudczig S, Vessey KA, Fletcher EL (2021) Retinal ganglion cell dysfunction in mice following acute intraocular pressure is exacerbated by P2X7 receptor knockout. Sci Rep 11:4184.

Wang Z, Bovik AC, Sheikh HR, Simoncelli EP (2004) Image quality assessment: from error visibility to structural similarity. IEEE Trans Image Process Publ IEEE Signal Process Soc 13:600–612.

Xu H, Jin N, Chuang J-Z, Zhang Z, Zhong X, Zhang Z, Sung C-H, Ribelayga CP, Fu Y (2022) Visual pigment-deficient cones survive and mediate visual signaling despite the lack of outer segments. Proc Natl Acad Sci U S A 119:e2115138119.

Yu W-Q, El-Danaf RN, Okawa H, Pacholec JM, Matti U, Schwarz K, Odermatt B, Dunn FA, Lagnado L, Schmitz F, Huberman AD, Wong ROL (2018) Synaptic Convergence Patterns onto Retinal Ganglion Cells Are Preserved despite Topographic Variation in Pre- and Postsynaptic Territories. Cell Rep 25:2017-2026.e3.

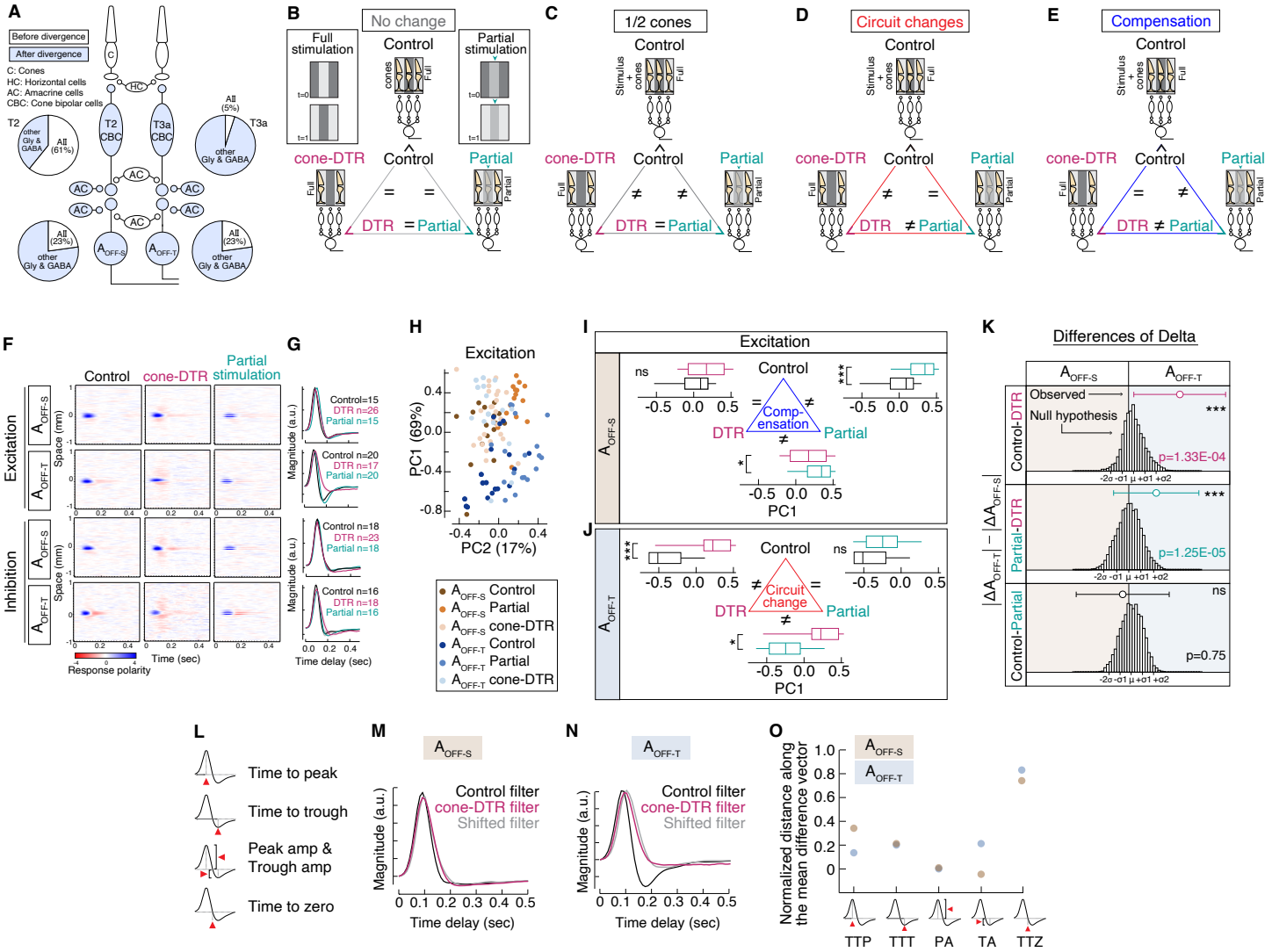

Figure 1. Partial cone loss causes differential temporal changes to A_{OFF} ganglion cell types. (A) Illustration of known cone pathways to $A_{OFF\text{-}S}$ and $A_{OFF\text{-}T}$ ganglion cells. Cones contact type 2 (T2) and 3a (T3a) OFF cone bipolar cells (CBCs), which receive different degrees of inhibitory inputs from AII and other amacrine cell types (top pie charts). T2 and T3a CBCs primarily contact $A_{OFF\text{-}S}$ and $A_{OFF\text{-}T}$ ganglion cells, respectively. Each ganglion cell type receives glycinergic and GABAergic inhibitory inputs and equivalent contributions from AII amacrine cells (bottom pie charts). If cone ablation affects circuits before divergence of the OFF pathways, then the following sites are implicated (white): cones, horizontal cells, common amacrine cells. If cone ablation affects circuits after divergence of the OFF channels, then the following locations are implicated (blue): bipolar cells (T2 or T3a), different amacrine cells that send their inputs to sustained or transient pathways. (B-E) Comparison of three conditions and their state of cones and the retinal circuit: (1) control condition has a full complement of cones and a control circuit (control); (2) DTR condition has half the cones and a DTR circuit (cone-DTR); (3) half stimulation condition has stimulation of half the cones and a control circuit (partial). Triangles represent comparisons among three conditions that would be interpreted as (B) no change, mechanisms caused by (C) half cone stimulation, (D) circuit changes, or (E) compensation. (F) Example spatio-temporal filters in response to a bar noise stimulus under three conditions for either $A_{OFF\text{-}S}$ (rows 1, 3) or $A_{OFF\text{-}T}$ (rows 2, 4) under voltage clamp for measuring excitation (rows 1-2) or inhibition (rows 3-4). (G) Average temporal filters of (odd rows) $A_{OFF\text{-}S}$ and (even rows) $A_{OFF\text{-}T}$ ganglion cells measuring excitation (rows 1-2) and inhibition (rows 3-4) for control (black), cone-DTR (magenta) and partial stimulation (green). (H) Each temporal filter is plotted as a function of its projection onto the first and second principal components from excitation. Variance captured by each principal component noted on the corresponding axis. $A_{OFF\text{-}S}$ plotted in warm colors and $A_{OFF\text{-}T}$ plotted in cool colors for the three conditions. (I-J) Box plots of first principal components (PC1) for each pairwise comparison of conditions for $A_{OFF\text{-}S}$ and $A_{OFF\text{-}T}$ ganglion cell excitation. Interpretation of

mechanisms in the triangle center. (K) Difference of deltas results for the null hypothesis for equivalent changes in the temporal filters between $A_{OFF\text{-}S}$ and $A_{OFF\text{-}T}$ ganglion cells in each comparison of conditions (bootstrapped distribution of 10,000 iterations with noted standard deviations) and the actual difference of deltas (circles with error bars). Significant difference from the null hypothesis displayed on the right. (L) Features extracted from temporal filters: time to peak (TTP), time to trough (TTT), peak amplitude (PA), trough amplitude (TA), and time to zero crossing (TTZ). (M-N) Average temporal filters under control and cone-DTR conditions for (M) $A_{OFF\text{-}S}$ and (N) $A_{OFF\text{-}T}$ ganglion cells, which show a significant difference, and a version of the control temporal filter shifted by multiple features to match the cone-DTR temporal filter. (O) Normalized distance between the temporal filter in control (ordinate = 0) and cone-DTR (ordinate = 1) when the control temporal filter is changed by each feature for $A_{OFF\text{-}S}$ (tan) and $A_{OFF\text{-}T}$ (blue) ganglion cells. P-values in box plots indicate rank sum comparison between each pair of conditions after correcting for multiple comparisons with the Holm method (I-J). P-values in difference of deltas plot (K) indicate significant differences between $A_{OFF\text{-}S}$ and $A_{OFF\text{-}T}$ ganglion cells from a permutation test with correction for multiple comparisons. The following asterisks indicate p values: * ≤ 0.05, ** ≤ 0.01, *** ≤ 0.005. See also Figures S2 and Dataset S1.

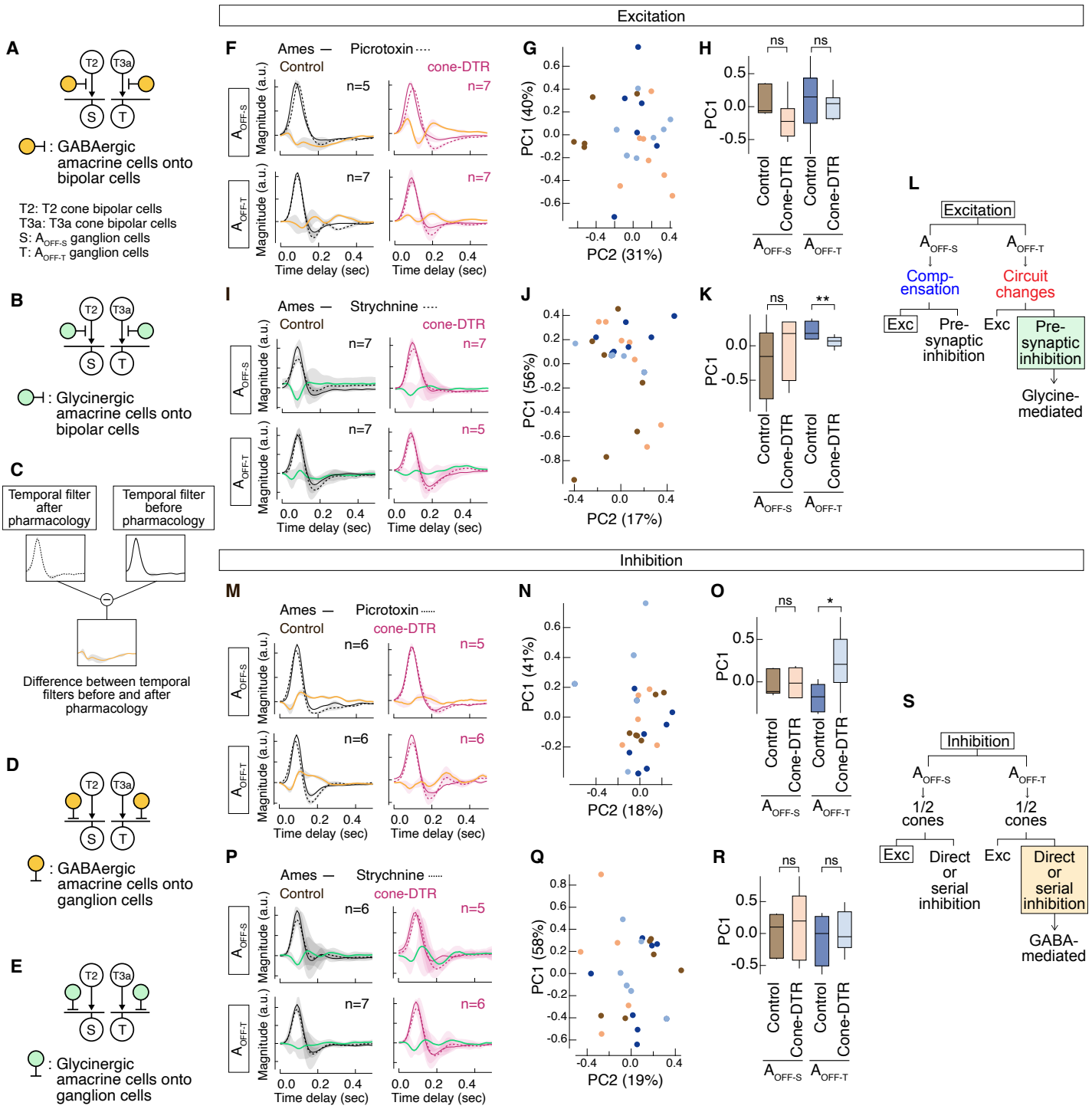

Figure 2. Partial cone loss causes presynaptic glycine and direct GABA inhibition to mediate changes in the cone-DTR temporal filters of $A_{OFF\text{-}T}$ ganglion cells. (A-B, D-E) Schematic of retinal pathways leading to the $A_{OFF\text{-}S}$ (left) and $A_{OFF\text{-}T}$ (right) ganglion cells and the circuit motifs for direct excitation (white), presynaptic inhibition from (A) GABA (yellow) or (B) glycine (green), and direct inhibition from (D) GABA (yellow) or (E) glycine (green) that would be blocked by (A, D) picrotoxin, an antagonist of $GABA_A$ and $GABA_C$ receptors, or (B, E) strychnine, an antagonist of glycine receptors. (C) Illustration of the difference filter computed by subtracting the temporal filters from after and before pharmacological application for each cell. (F, I, M, P) Average temporal filters from (F, I) excitatory and (M, P) inhibitory currents of $A_{OFF\text{-}S}$ (odd rows) and $A_{OFF\text{-}T}$ (even rows) ganglion cells in control (left) and cone-DTR (right) retinas under Ames (solid line) and (F, M) 100μM picrotoxin or (I, P) 5 μM strychnine (dashed line) as well as the difference between Ames and (F, M) picrotoxin (yellow) or (I, P) strychnine (green). (G, J, N, Q) First and second principal components from (G, J)

excitatory and (N, Q) inhibitory temporal filter differences between (G, N) picrotoxin and Ames or (J, Q) strychnine and Ames of each $A_{OFF\text{-}S}$ (warm colors) or $A_{OFF\text{-}T}$ (cool colors; refer to box plot colors in H for legend). Variance captured by each principal component noted on the corresponding axis. (H, K, O, R) Box plots of first principal components (PC1) across cell types and conditions for the differences between (H, O) Ames and picrotoxin or (K, R) Ames and strychnine from (H, K) excitation temporal filters and (O, R) inhibition temporal filters. (L, S) Results of the comparison of PC1 and the interpretation of mechanisms for (L) excitatory temporal filters and (S) inhibitory temporal filters. P-values in box plots indicate rank sum comparison between each pair of conditions; p-values are corrected for multiple comparisons with the Holm method (H, K, O, R). See also Dataset S1.

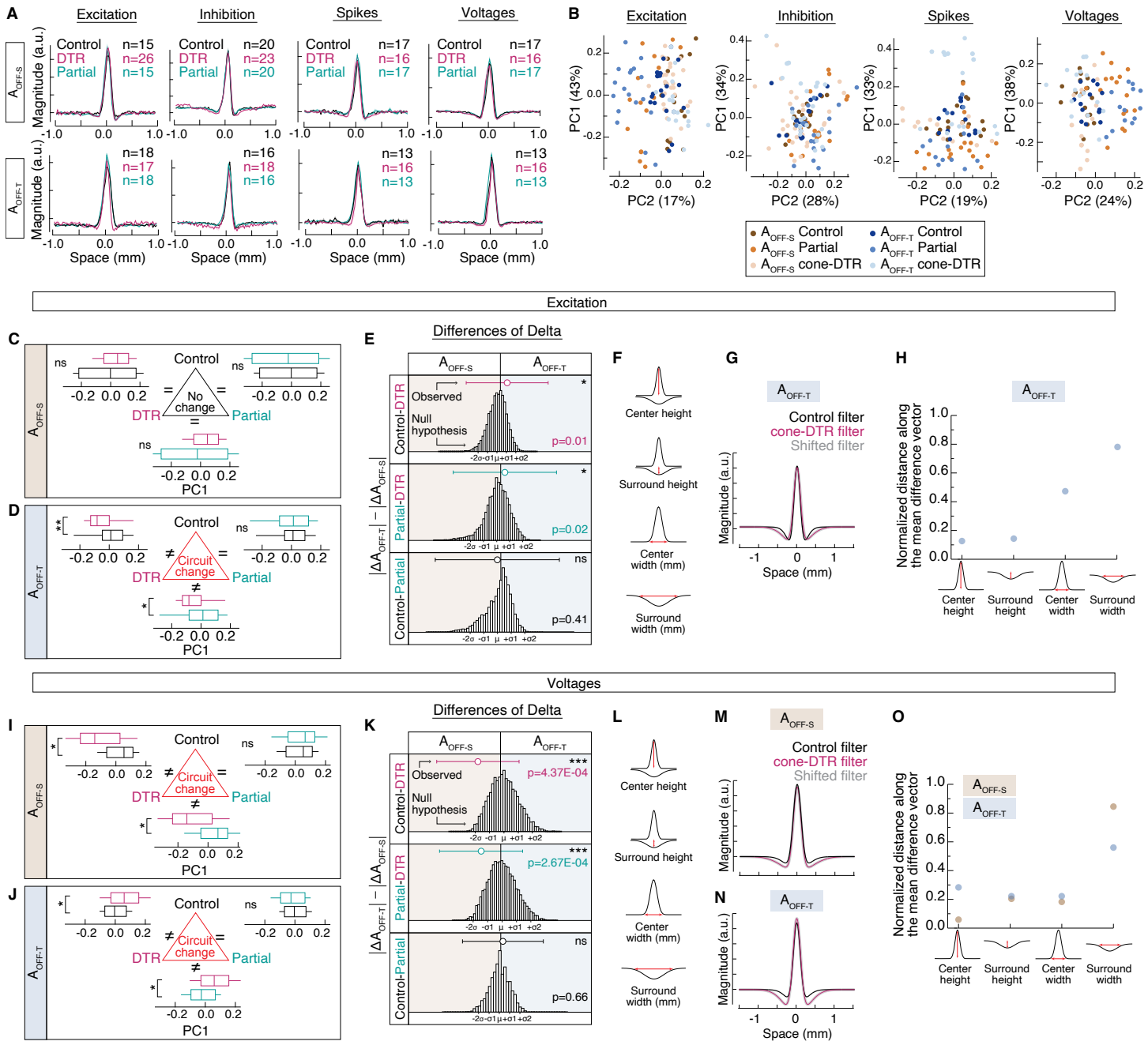

Figure 3. Partial cone loss causes differential changes in spatial filters of A_{OFF} ganglion cell types. (A) Average spatial filters from excitation, inhibition, subthreshold voltages and spikes of (top) $A_{OFF\text{-}S}$ and (bottom) $A_{OFF\text{-}T}$ ganglion cells in control (black), cone-DTR (magenta) and partial stimulation (green). (B) Projections onto the first and second principal components for the spatial filters of each $A_{OFF\text{-}S}$ (warm colors) or $A_{OFF\text{-}T}$ (cool colors) for the three conditions from excitation, inhibition, voltages and spikes. Variance captured by each principal component noted on the corresponding axis. (C-D, I-J) Box plots of first principal components (PC1) for (C, I) $A_{OFF\text{-}S}$ and (D, J) $A_{OFF\text{-}T}$ ganglion cells between conditions from (C-D) excitation and (I-J) voltages, which showed significant differences across conditions. Interpretation of mechanisms in the triangle centers. (E, K) Difference of deltas results for the null hypothesis for equivalent changes in the spatial filters between $A_{OFF\text{-}S}$ and $A_{OFF\text{-}T}$ ganglion cells in each comparison of conditions (bootstrapped distribution of 10,000 iterations with noted standard deviations) and the actual difference of deltas (circles with error bars) for (E) excitation and (K) voltages. Significant difference from the null hypothesis displayed on the right. (F, L) Features extracted from spatial filters: center height, surround height, center width, and surround width for (F) excitation and (L) voltages. (G, M-N) Average spatial filters under control and cone-DTR conditions for (G) $A_{OFF\text{-}T}$ ganglion cell

excitation and (M) $A_{OFF\text{-}S}$ and (N) $A_{OFF\text{-}T}$ ganglion cell voltages, which show a significant difference between control vs. cone-DTR, and a version of the control spatial filter shifted by multiple parameters to match the cone-DTR spatial filter. (H, O) Normalized distance between the spatial filter in control (ordinate = 0) and cone-DTR (ordinate = 1) when the control spatial filter is changed by each parameter for (H) $A_{OFF\text{-}T}$ ganglion cell excitation and (O) $A_{OFF\text{-}S}$ and $A_{OFF\text{-}T}$ ganglion cell voltages. P-values in box plots indicate rank sum comparison between each pair of conditions; p-values are corrected for multiple comparisons with the Holm method (C-D, I-J). P-values in the difference of deltas plots indicate significant differences between $A_{OFF\text{-}S}$ and $A_{OFF\text{-}T}$ ganglion cells from a permutation test with correction for multiple comparisons (E, K). See also Figure S3 and Dataset S1.

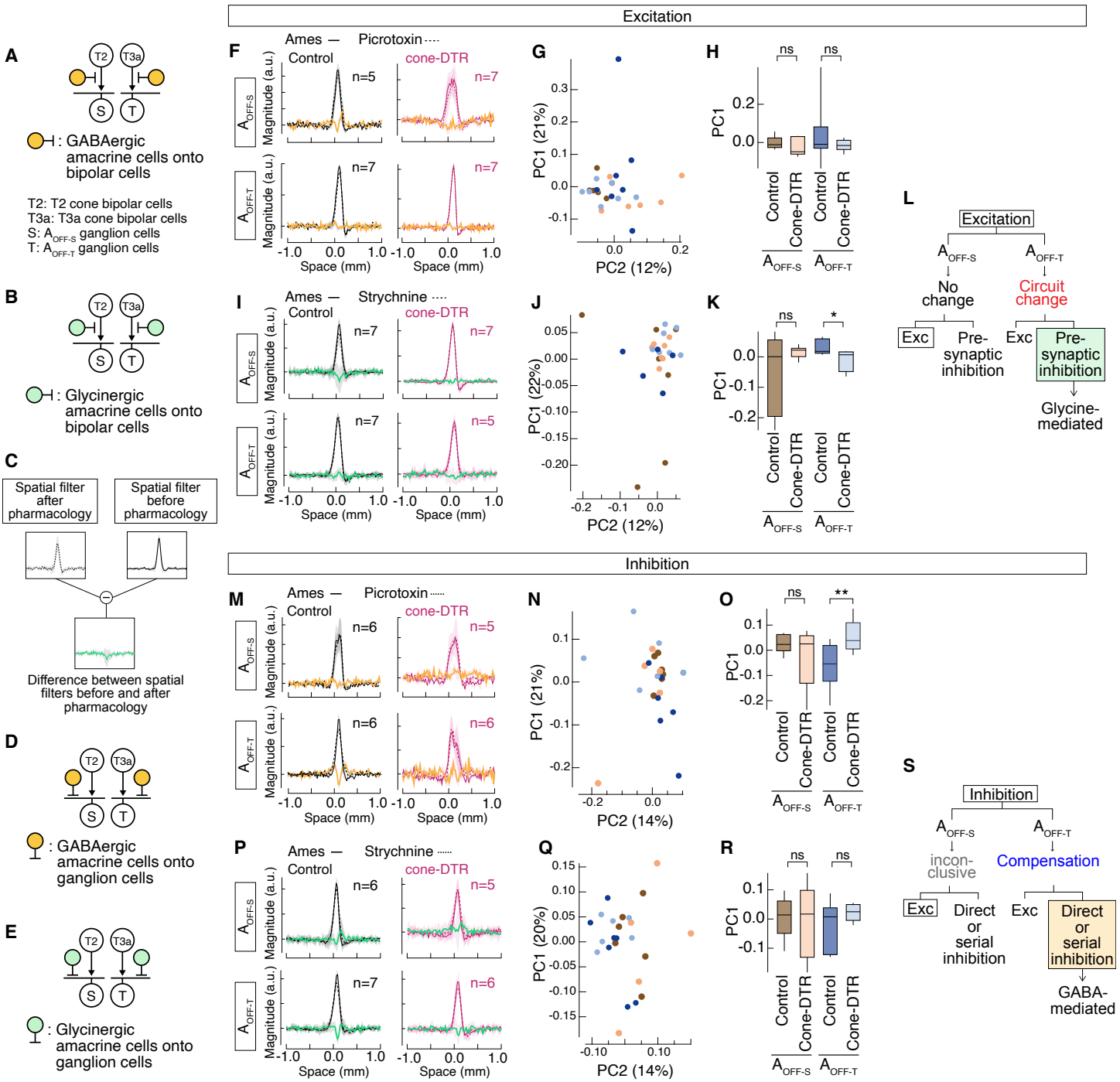

Figure 4. Partial cone loss causes excitation and direct GABAergic and glycinergic inhibition to mediate changes in the cone-DTR spatial filters of $A_{OFF\text{-}T}$ ganglion cells. (A-B, D-E) Schematic of retinal pathways leading to the (left) $A_{OFF\text{-}S}$ and (right) $A_{OFF\text{-}T}$ ganglion cells and the circuit motifs for direct excitation (white), presynaptic inhibition from (A) GABA (yellow) or (B) glycine (green), and direct inhibition from (D) GABA (yellow) or (E) glycine (green) that would be blocked by (A, D) picrotoxin, an antagonist of $GABA_A$ and $GABA_C$ receptors, or (B, E) strychnine, an antagonist of glycine receptors. (C) Illustration of the difference filter computed from subtracting the spatial filters from after and before pharmacological application for each cell. (F, I, M, P) Average spatial filters from (F, I) excitatory and (M, P) inhibitory currents of $A_{OFF\text{-}S}$ (odd rows) and $A_{OFF\text{-}T}$ (even rows) ganglion cells in control (left) and cone-DTR (right) retinas under Ames (solid line) and (F, M) 100μM picrotoxin or (I, P) 5 μM strychnine (dashed line) as well as the difference between Ames and (F, M) picrotoxin (yellow) or (I, P) strychnine (green). (G, J, N, Q) First and second principal components from (G, J) excitatory and (N, Q) inhibitory spatial filter differences between (G, N) picrotoxin and Ames or (J, Q)

strychnine and Ames of each $A_{OFF\text{-}S}$ (warm colors) or $A_{OFF\text{-}T}$ (cool colors; refer to box plot colors in H for legend). Variance captured by each principal component noted on the corresponding axis. (H, K, O, R) Box plots of first principal components (PC1) across cell types and conditions for the differences between (H, O) picrotoxin and Ames or (K, R) strychnine and Ames from (H, K) excitation spatial filters and (O, R) inhibition spatial filters. (L, S) Results of the comparison of PC1 and the interpretation of mechanisms for (L) excitatory and (S) inhibitory spatial filters. P-values in box plots indicate rank sum comparison between each pair of conditions; p-values are corrected for multiple comparisons with the Holm method (H, K, O, R). See also Dataset S1.

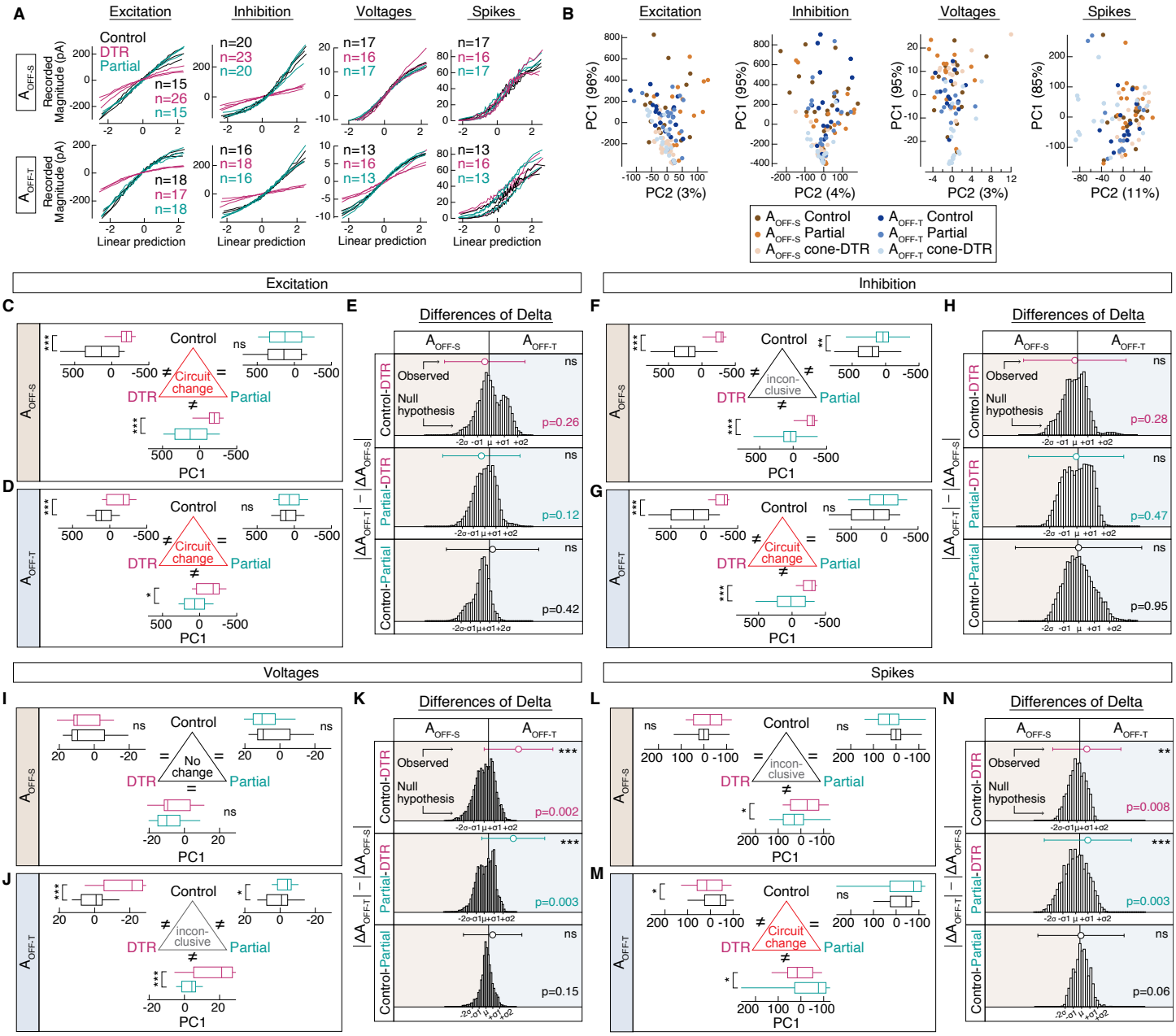

Figure 5. Partial cone loss affects nonlinearities at multiple levels leading to partial recovery of A_{OFF} ganglion cell outputs. (A) Three exemplar nonlinearities from control (black), cone-DTR retina (magenta), and partial stimulation (green) for excitation, inhibition, subthreshold voltages, and spikes from individual (top) $A_{OFF\text{-}S}$ and (bottom) $A_{OFF\text{-}T}$ ganglion cells. (B) First and second principal components for the nonlinearity of each $A_{OFF\text{-}S}$ (warm colors) or $A_{OFF\text{-}T}$ (cool colors) for the three conditions from excitation, inhibition, voltages, and spikes. Variance captured by each principal component noted on the corresponding axis. (C-D, F-G, I-J, L-M). Box plots of first principal components (PC1) for $A_{OFF\text{-}S}$ and $A_{OFF\text{-}T}$ ganglion cells between conditions from (C-D) excitation, (F-G) inhibition, (I-J) voltages, (L-M) spikes. Interpretation of mechanisms in the triangle centers. (E, H, K, N) Difference of deltas results for the null hypothesis for equivalent changes in the nonlinearity between $A_{OFF\text{-}S}$ and $A_{OFF\text{-}T}$ ganglion cells in each comparison of conditions (bootstrapped distribution of 10,000 iterations with noted standard deviations) and the actual difference of deltas (circles with error bars) for (E) excitation, (H) inhibition, (K) voltages, and (N) spikes. Significant difference from the null hypothesis displayed on the right. P-values in box plots indicate rank sum comparison between each pair of conditions; p-values are corrected for multiple comparisons with the Holm method (C-D, F-G, I-J, L-M). P-values in the difference of deltas plots from a permutation test with correction for multiple comparisons (E, H, K, N). See also Figures 6, S4 and Dataset S1.

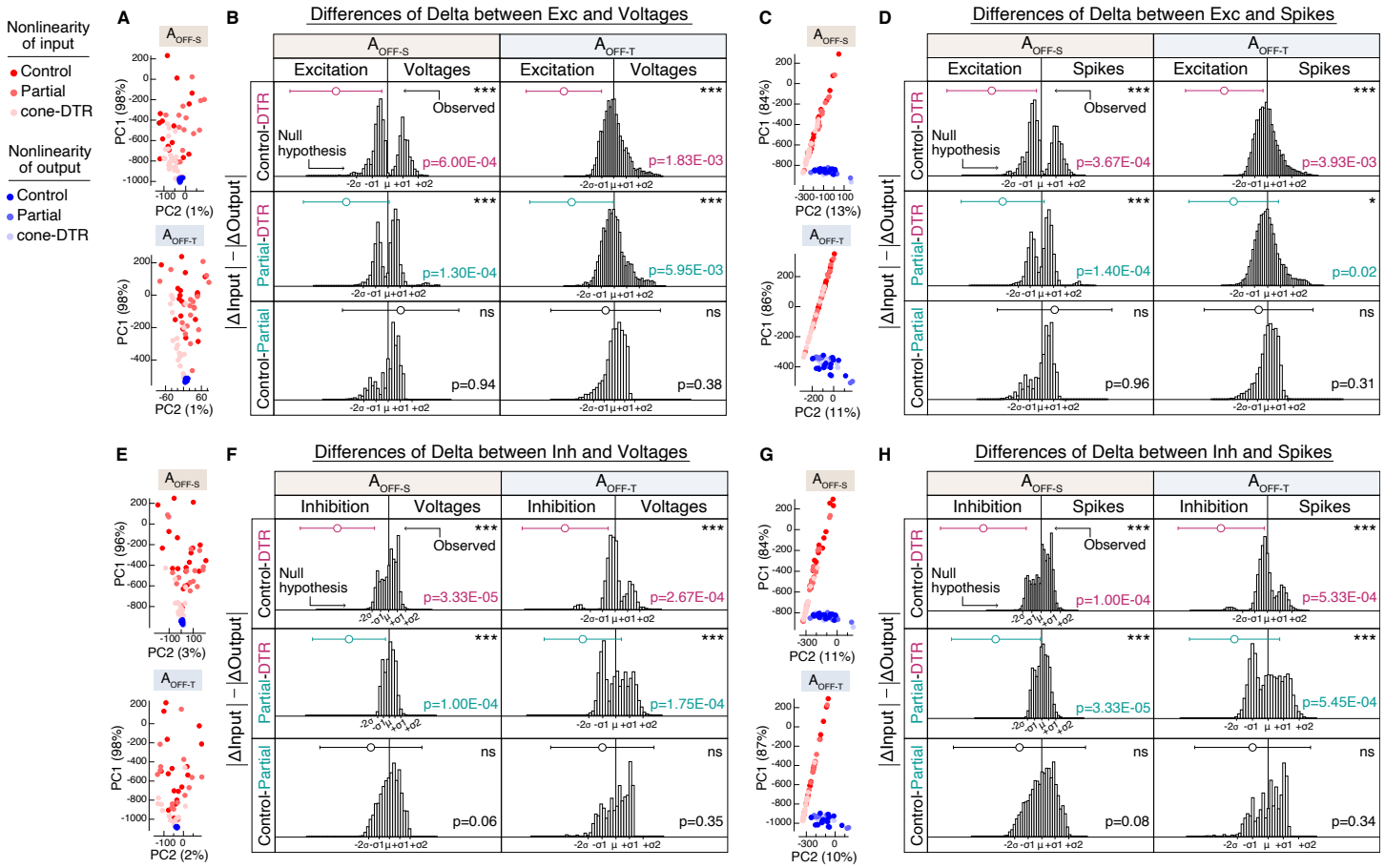

Figure 6. Partial cone loss has a differential impact on nonlinearities of input currents vs. output voltages and spikes. (A, C, E, G) Principal component analysis was performed on the nonlinearities for (A) excitation and subthreshold voltages, (D) excitation and spikes, (E) inhibition and subthreshold voltages, (G) inhibition and spikes. (B, D, F, H) Using the projection onto the first principal component of nonlinearities across conditions, we analyzed the difference of deltas to determine differences between inputs vs. outputs within each cell type. P-values in the difference of deltas plots from a permutation test with correction for multiple comparisons (B, D, F, H). See also Dataset S1.

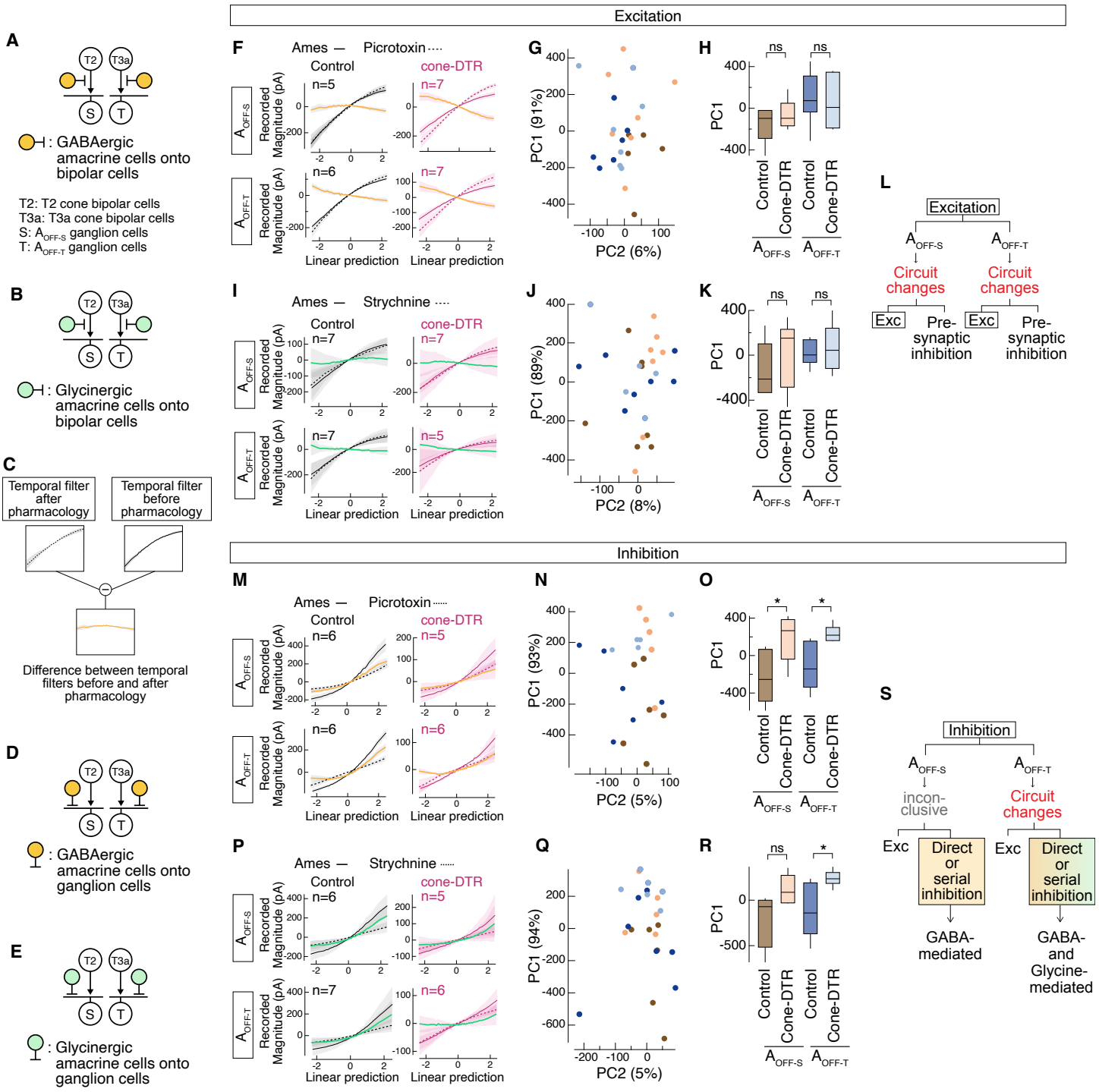

Figure 7. Partial cone loss causes excitation, direct GABA and glycine inhibition to mediate changes in the cone-DTR nonlinearities of A_{OFF} ganglion cells. (A-B, D-E) Schematic of retinal pathways leading to the (left) A_{OFF-S} and (right) A_{OFF-T} ganglion cells and the circuit motifs for direct excitation (white), presynaptic inhibition from (A) GABA (yellow) or (B) glycine (green), and direct inhibition from (D) GABA (yellow) or (E) glycine (green) that would be blocked by (A, D) picrotoxin, an antagonist of $GABA_A$ and $GABA_C$ receptors, or (B, E) strychnine, an antagonist of glycine receptors. (C) Illustration of the difference nonlinearity computed from subtracting the nonlinearities from after and before pharmacological application for each cell. (F, I, M, P) Average nonlinearities from (F, I) excitatory and (M, P) inhibitory currents of A_{OFF-S} (odd rows) and A_{OFF-T} (even rows) ganglion cells in control (left) and cone-DTR (right) retinas under Ames (solid line) and (F, M) 100μM picrotoxin or (I, P) 5 μM strychnine (dashed line) as well as the difference between Ames and (F, M) picrotoxin (yellow) or (I, P) strychnine (green). (G, J, N, Q) First and second principal components for the (G, J) excitatory

and (N, Q) inhibitory nonlinearity differences between (G, N) picrotoxin and Ames or (J, Q) strychnine and Ames of each $A_{OFF\text{-}S}$ (warm colors) or $A_{OFF\text{-}T}$ (cool colors; refer to box plot colors in H for legend). Variance captured by each principal component noted on the corresponding axis. (H, K, O, R) Box plots of first principal components (PC1) across cell types and conditions for the differences between (H, O) picrotoxin and Ames or (K, R) strychnine and Ames from (H, K) excitation nonlinearities and (O, R) inhibition nonlinearities. (L, S) Results of the comparison of PC1 and the interpretation of mechanisms for (L) excitatory and (S) inhibitory nonlinearities. P-values in box plots indicate rank sum comparison between each pair of conditions; p-values are corrected for multiple comparisons with the Holm method (H, K, O, R). See also Dataset S1.

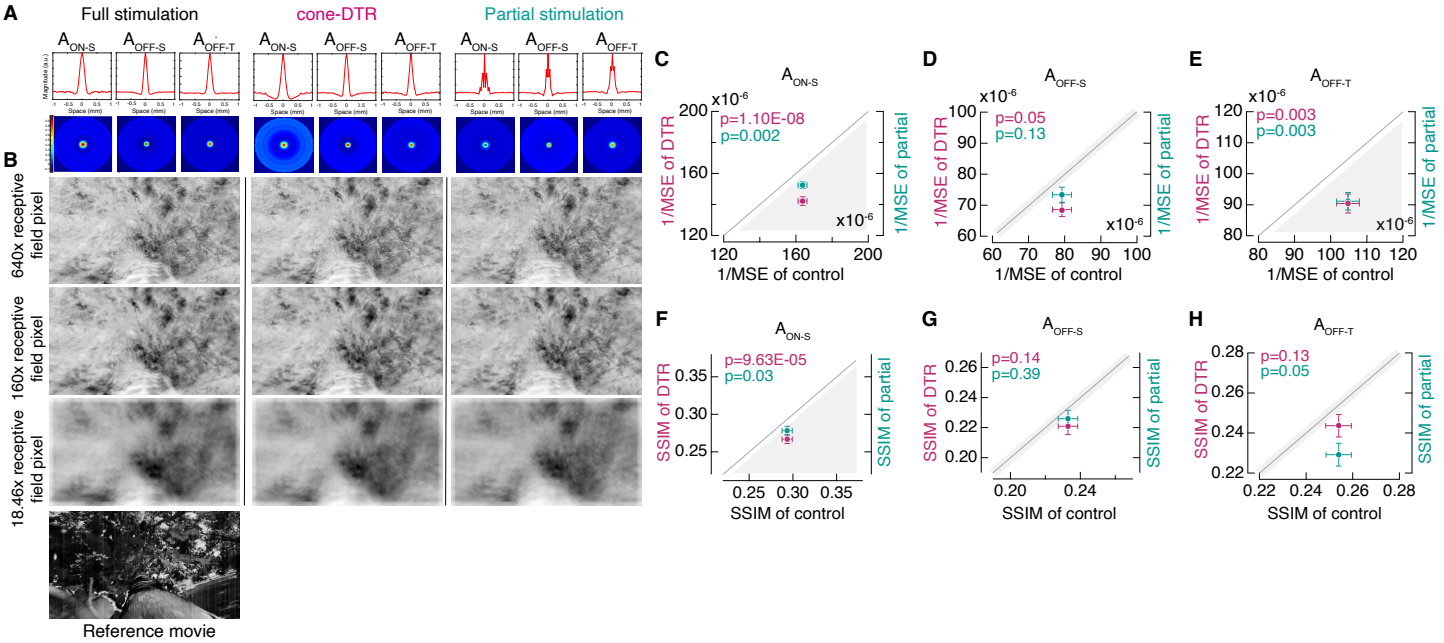

Figure 8. Natural movies filtered by the measured spatiotemporal receptive fields following partial cone loss are perceptually similar to those filtered by control retina. (A) Average linear spatial filters from bar noise stimuli (top) and 3D receptive fields (bottom) of $A_{ON\text{-}S}$, $A_{OFF\text{-}S}$, and $A_{OFF\text{-}T}$ ganglion cells under the following conditions: (1) full stimulation of control retina, (2) cone-DTR retina, and (3) partial stimulation of control retina. (B) Example frame of movies resulting from convolution of a reference movie (bottom) with each of three spatiotemporal filters at movie sizes 640, 160, 18.46 times the receptive field size. (C-E) Non-perceptual similarity index (1/MSE) averaged across movie-to-receptive field pixel ratios in conditions of control (abscissa), cone-DTR (left ordinate; magenta), and partial stimulation (right ordinate; green) for (C) $A_{ON\text{-}S}$, (D) $A_{OFF\text{-}S}$, and (E) $A_{OFF\text{-}T}$ ganglion cells. (F-H) Structural similarity index (SSIM) of convolved movies with the reference movies averaged across movie-to-receptive field pixel ratios in three conditions of control (abscissa), cone-DTR (left ordinate; magenta), and partial stimulation (right ordinate; green) for (F) $A_{ON\text{-}S}$, (G) $A_{OFF\text{-}S}$, and (H) $A_{OFF\text{-}T}$ ganglion cells. P-values from two-way ANOVA to compare differences between convolved movies under either cone-DTR or partial stimulation with the movies convolved by the control condition. Gray regions mark whether the p-value is not significant (along the line of slope unity) or significant (gray triangle). See also Figure S6 and Dataset S1.

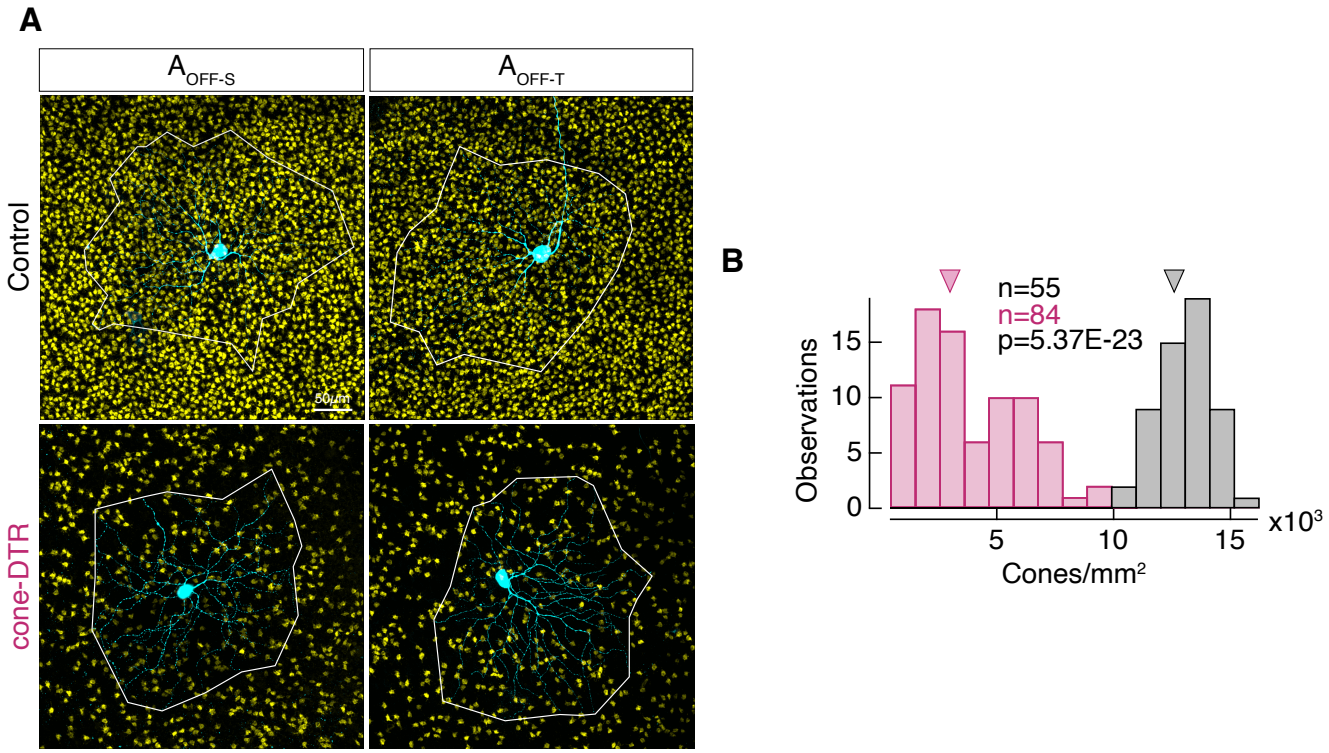

Figure S1. Simian diphtheria toxin receptor system ablates a partial population of cones in the mouse retina. (A) Confocal images of cone pedicles labeled with cone arrestin in control and cone-DTR conditions in dorsal-nasal retina of $A_{OFF\text{-}S}$ and $A_{OFF\text{-}T}$ ganglion cells. The bounding box (white line) shows the region of the dendritic field of the cell. (B) Histogram of cone densities: control 13,007.700±1,581.84 cones/mm^2; cone-DTR 4,047.030±280.259 cones/mm^2; median±IQR, p=5.37E-23, rank sum. Arrowheads indicate medians. n represents the number of images. Number of animals: control=39, cone-DTR=47.

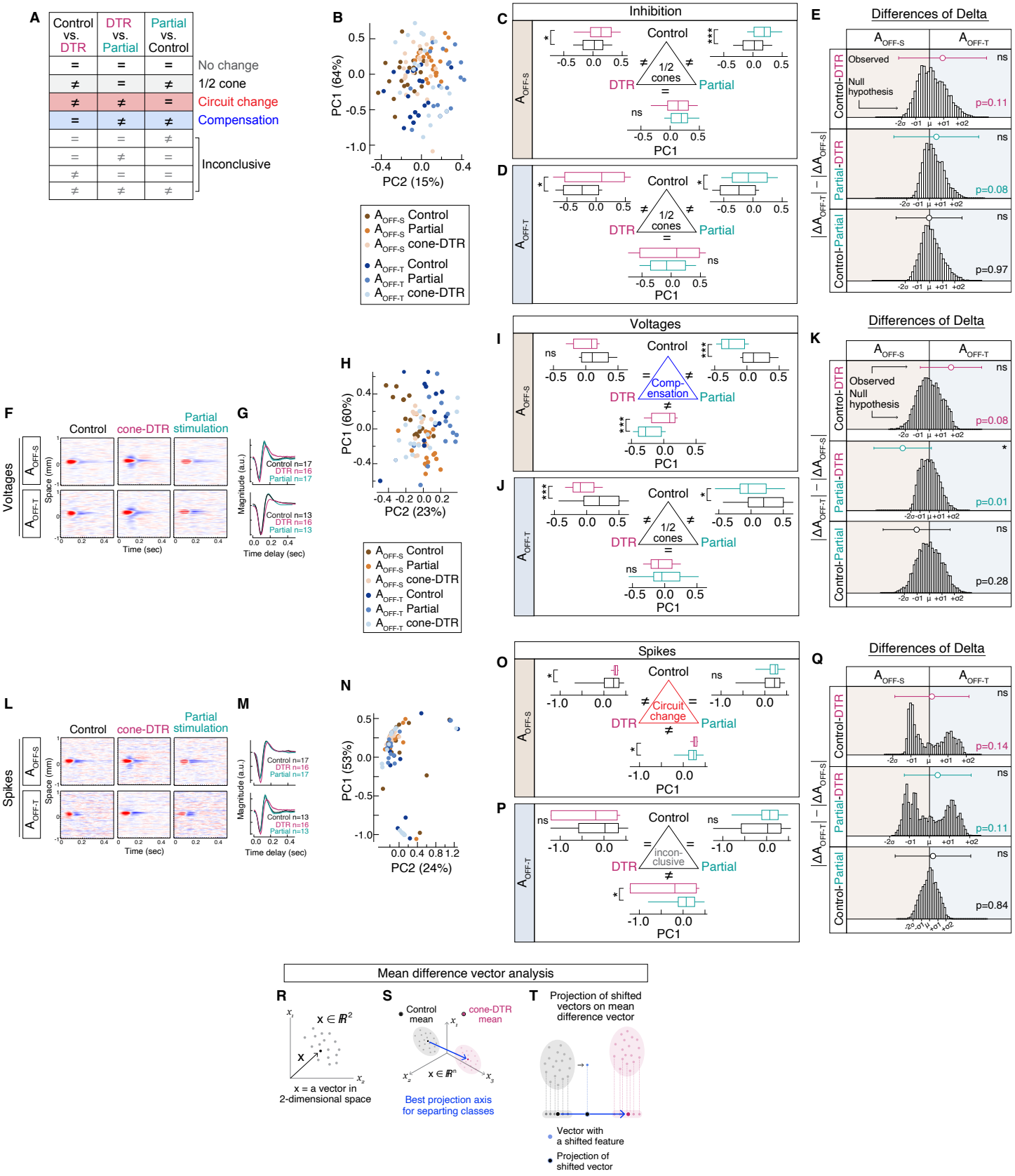
A
Control vs. DTR
DTR vs. Partial
Partial vs. Control
No change
1/2 cone
Circuit change
Compensation
Inconclusive
B
PC1 (64%)
PC2 (15%)
Control
Partial
cone-DTR
C
Inhibition
Control
DTR
Partial
1/2 cones
PC1
D
E
Differences of Delta
Observed
Null hypothesis
p=0.11
p=0.08
p=0.97
F
Voltages
Control
cone-DTR
Partial stimulation
Space (mm)
Time (sec)
G
Magnitude (a.u.)
Time delay (sec)
H
PC1 (60%)
PC2 (23%)
I
Voltages
Comp-ensation
J
K
Differences of Delta
p=0.08
p=0.01
p=0.28
L
Spikes
M
N
PC1 (53%)
PC2 (24%)
O
Spikes
Circuit change
P
incon-clusive
Q
Differences of Delta
p=0.14
p=0.11
p=0.84
Mean difference vector analysis
R
x = a vector in 2-dimensional space
S
Control mean
cone-DTR mean
Best projection axis for separting classes
T
Projection of shifted vectors on mean difference vector
Vector with a shifted feature
Projection of shifted vector

Figure S2. Following partial cone loss, kinetics of temporal filters from inhibitory currents, subthreshold voltages and spikes are similar between A_{OFF} ganglion cell types. A) Table of possible results in pairwise comparisons of three conditions as the same (=) or different (≠) and the interpretation. Other combinations of comparisons not depicted include additional inconclusive results. (B) First and second principal components of the inhibitory temporal filters from each A_{OFF-S} (warm colors) or A_{OFF-T} (cool colors) across three conditions. Variance captured by each principal component noted on the corresponding axis. (C-D) Box plot of first principal components (PC1) for (C) A_{OFF-S} and (D) A_{OFF-T} ganglion cells between conditions. Interpretation of mechanisms in the triangle centers. (E) Difference of deltas results for the null hypothesis for equivalent changes in inhibitory temporal filters between A_{OFF-S} and A_{OFF-T} ganglion cells in each comparison of conditions (bootstrapped distribution of 10,000 iterations with noted standard deviations) and the actual difference of deltas (circles with error bars). Significant difference from the null hypothesis displayed on the right. P-values in box plots indicate rank sum comparison between each pair of conditions; p-values are corrected for multiple comparisons with the Holm method (C-D). P-values in the difference of deltas plot from a permutation test with correction for multiple comparisons (E). (F, L) Example spatio-temporal filters in response to a bar noise stimulus under three conditions for either A_{OFF-S} (top) or A_{OFF-T} (bottom) under current clamp for measuring (F) voltages and (L) spikes. (G, M) Average temporal filters from (G) voltages (M) spikes of (top) A_{OFF-S} and (bottom) A_{OFF-T} ganglion cells in control, cone-DTR, and partial stimulation of control retina. (H, N) First and second principal components of (H) voltage and (N) spike temporal filters from each A_{OFF-S} (warm colors) or A_{OFF-T} (cool colors) for the three conditions. Variance captured by each principal component noted on the corresponding axis. (I-J, O-P) Box plots of first principal components (PC1) for (I, J) A_{OFF-S} and (O, P) A_{OFF-T} ganglion cells between conditions for (I-J) voltages, and (O-P) spikes. Interpretation of mechanisms in triangle centers. (K, Q) Difference of deltas results for the null hypothesis for equivalent changes in temporal filters from (K voltages and (Q) spikes between A_{OFF-S} and A_{OFF-T} ganglion cells in each comparison of conditions (bootstrapped distribution of 10,000 iterations with noted standard deviations) and the actual difference of deltas (circles with error bars). Significant difference from the null hypothesis displayed on the right. P-values in box plots indicate rank sum comparison between each pair of conditions; p-values are corrected for multiple comparisons with the Holm method (I-J, O-P). P-values in difference of deltas plots from a permutation test with correction for multiple comparisons (K, Q). (R-T) Schematic of temporal filters from each cell plotted in n-dimensional space (F), followed by identifying the mean difference vector between conditions, e.g., control vs. cone-DTR (S), and finally a projection of how shifting the temporal filter according to specific features, e.g., time to peak, time to trough, etc., moves along the vector that discriminates the two conditions of control vs. cone-DTR (T). See also Dataset S1.

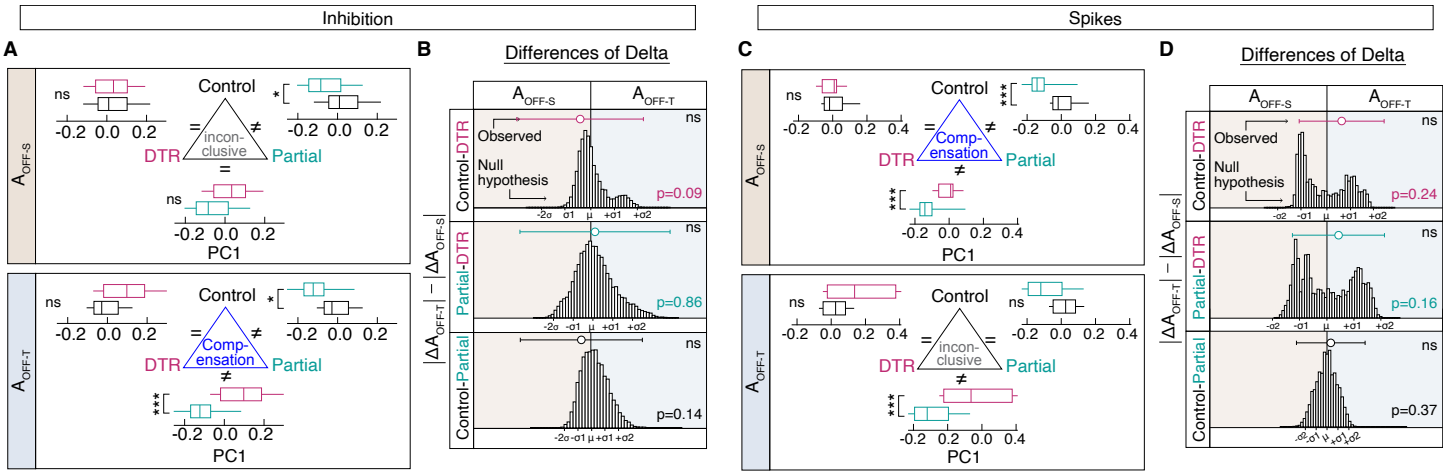

Figure S3. After partial cone loss, inhibitory and spike spatial filters are similar between A_{OFF} ganglion cell types. (A, C) Box plots of first principal components (PC1) of spatial filters from (A) inhibition and (C) spikes from $A_{OFF\text{-}S}$ (top) and $A_{OFF\text{-}T}$ (bottom) ganglion cells across conditions. Interpretation of mechanisms for excitation in the triangle centers. (B, D) Difference of deltas results for the null hypothesis for equivalent changes in spatial filters from (B) inhibition and (D) spikes between $A_{OFF\text{-}S}$ and $A_{OFF\text{-}T}$ ganglion cells in each comparison of conditions (bootstrapped distribution of 10,000 iterations with noted standard deviations) and the actual difference of deltas (circles with error bars). Significant difference from the null hypothesis displayed on the right. P-values in box plots indicate rank sum comparison between each pair of conditions; p-values are corrected for multiple comparisons with the Holm method (A, C). P-values in difference of deltas plots from a permutation test with correction for multiple comparisons (B, D). See also Dataset S1.

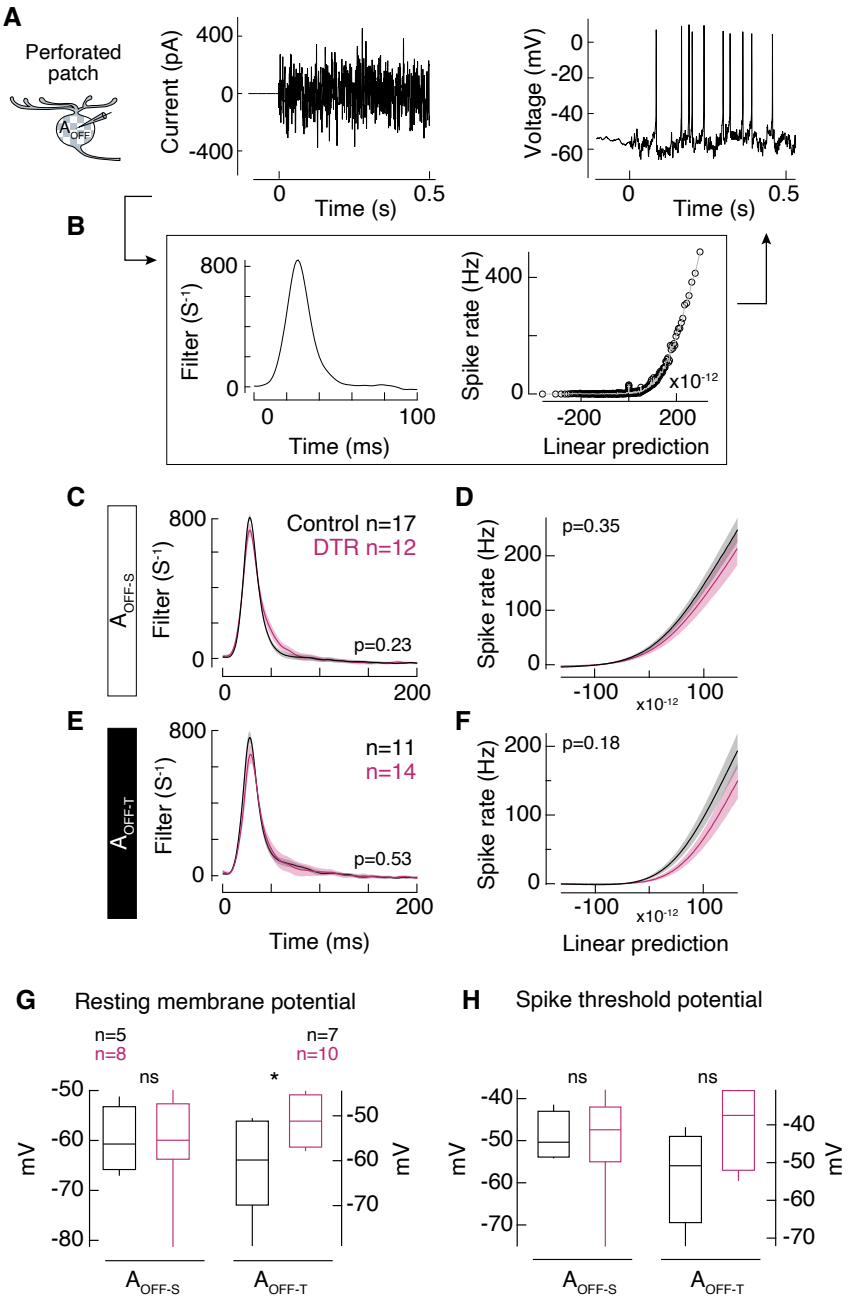

Figure S4. Intrinsic excitabilities of $A_{OFF\text{-}S}$ and $A_{OFF\text{-}T}$ ganglion cells are maintained while resting membrane potential of $A_{OFF\text{-}T}$ ganglion cells is depolarized after partial cone loss. (A) A_{OFF} ganglion cells recorded by perforated patch, and current was injected (left) and spikes were recorded (right) on a mean background. (B) Current-to-spike transformation is captured by a time-reversed spike-triggered average (left) and nonlinearity (right), which is fit with a sigmoid function (grey). (C-F) Averages of time-reversed spike-triggered averages and nonlinearities (C-D) of $A_{OFF\text{-}S}$ and (E-F) $A_{OFF\text{-}T}$ ganglion cells. (G) Resting membrane potential and (H) spike threshold potential were measured from $A_{OFF\text{-}S}$ and $A_{OFF\text{-}T}$ ganglion cells during whole-cell patch-clamp recordings. $A_{OFF\text{-}T}$ ganglion cells of cone-DTR retina were more depolarized than $A_{OFF\text{-}S}$ ganglion cells while spike thresholds were maintained across cell types. Box plots show median with IQR and whiskers from 10% to 90% of the data. n represents the number of cells. See also Dataset S1.

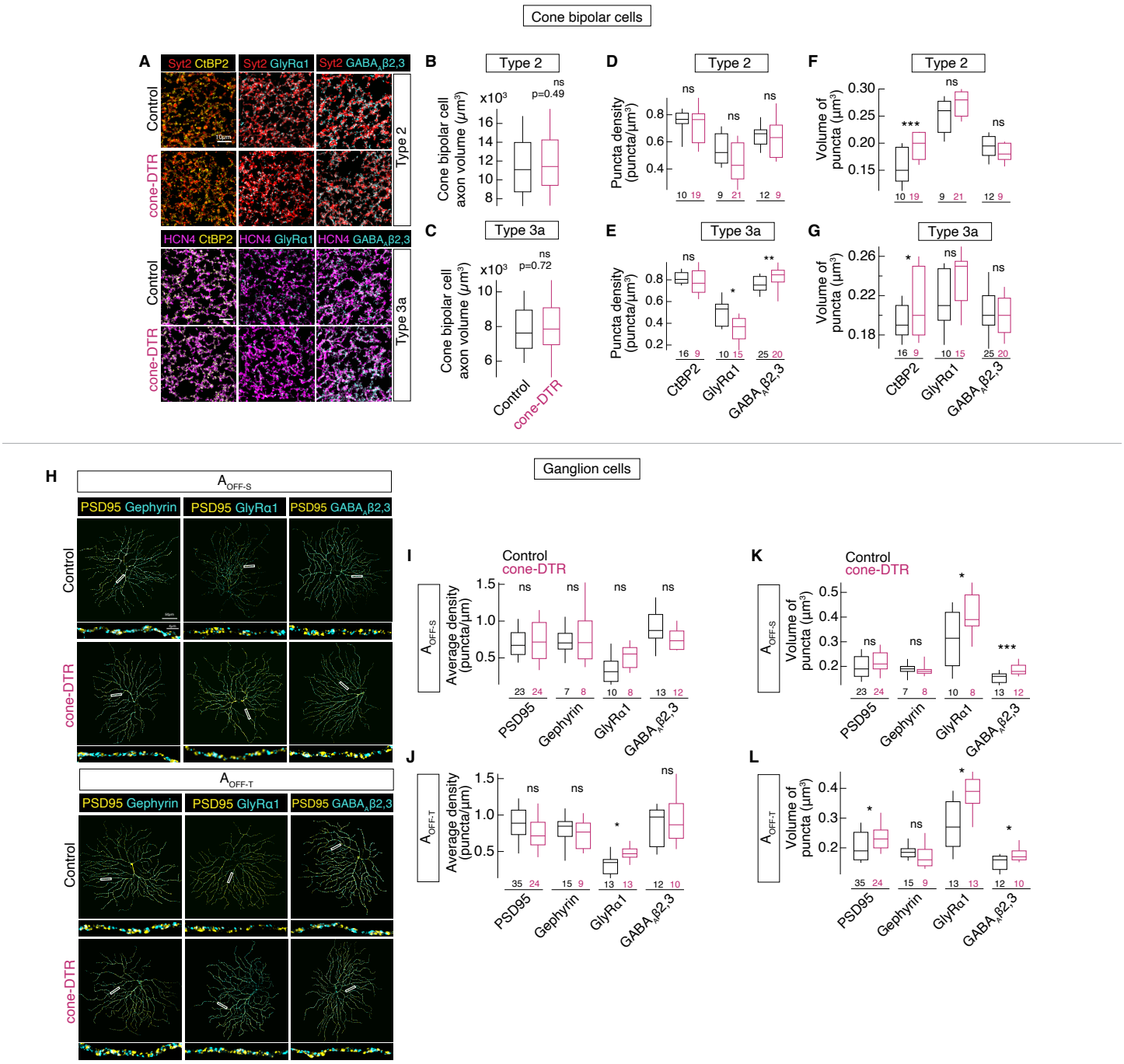

Figure S5. Excitatory and inhibitory synapses change in OFF pathways following partial cone loss. (A) *En face* confocal images of T2 (rows 1-2) and T3a (rows 3-4) OFF CBC axons as labeled by synaptotagmin 2 (Syt2) and HCN4 (magenta) with CtBP2 (yellow) for excitatory output synapses, GlyRα1 for glycine receptor alpha-1, and GABA$_A$β2,3 (cyan) for GABA$_A$ receptor subunit beta 2-3 in control (rows 1, 3) and cone-DTR (rows 2, 4) retina. (B-C) The volume of cone bipolar cell axon terminals in cone-DTR retina remained constant. (D-G) While the puncta density of ribbon synapses was maintained in the axons of both cone bipolar cell populations (D-E), we found an increased volume of CtBP2 in both bipolar cell types (F-G). In contrast to the enlarged volume of excitatory synapses, that of inhibitory synapses remained unchanged. Interestingly, we found differential changes in the density of GlyRα1 and GABA$_A$Rβ2,3 in T3a cone bipolar cell (D-E). These results demonstrate common adjustments of excitatory synaptic ribbons in response to partial cone loss whereas inhibitory synapses potentially undergo differential changes between T2 and T3a cone bipolar cells. (H) *En face* confocal images of control A$_{OFF-S}$ (rows 1-2) and A$_{OFF-T}$ (rows 3-4) ganglion cells labeled with PSD95, GlyRα1, gephyrin, and GABA$_A$β2,3 and in cone-DTR retina. Insets show a stretch of dendrites with

puncta for rectangles in main images. (I-J) Average puncta volume of PSD95, gephyrin, GlyRα1, and $GABA_A$β2,3 within the dendrites of (I) A_{OFF-S} and (J) A_{OFF-T} ganglion cells. While the volume and density of PSD95 remained constant in A_{OFF-S} ganglion cells, A_{OFF-T} ganglion cells showed increased PSD95 puncta size (I-J). We also found increased volume of GlyRα1 and $GABA_A$Rβ2,3 clusters in both ganglion cell types (I-J). (K-L) Average linear density of PSD95, gephyrin, GlyRα1, and $GABA_A$β2,3 within the dendrites of (K) A_{OFF-S} and (L) A_{OFF-T} ganglion cells. Despite a common increase in the volume of inhibitory receptors, A_{OFF} ganglion cells exhibit differential changes to synaptic density (K-L). Density and volume of gephyrin were maintained in both cell types in cone-DTR retina. Box plots show median with IQR and whiskers from 10% to 90% of the data. P-values indicate rank sum comparison between cell types. See also Dataset S1.

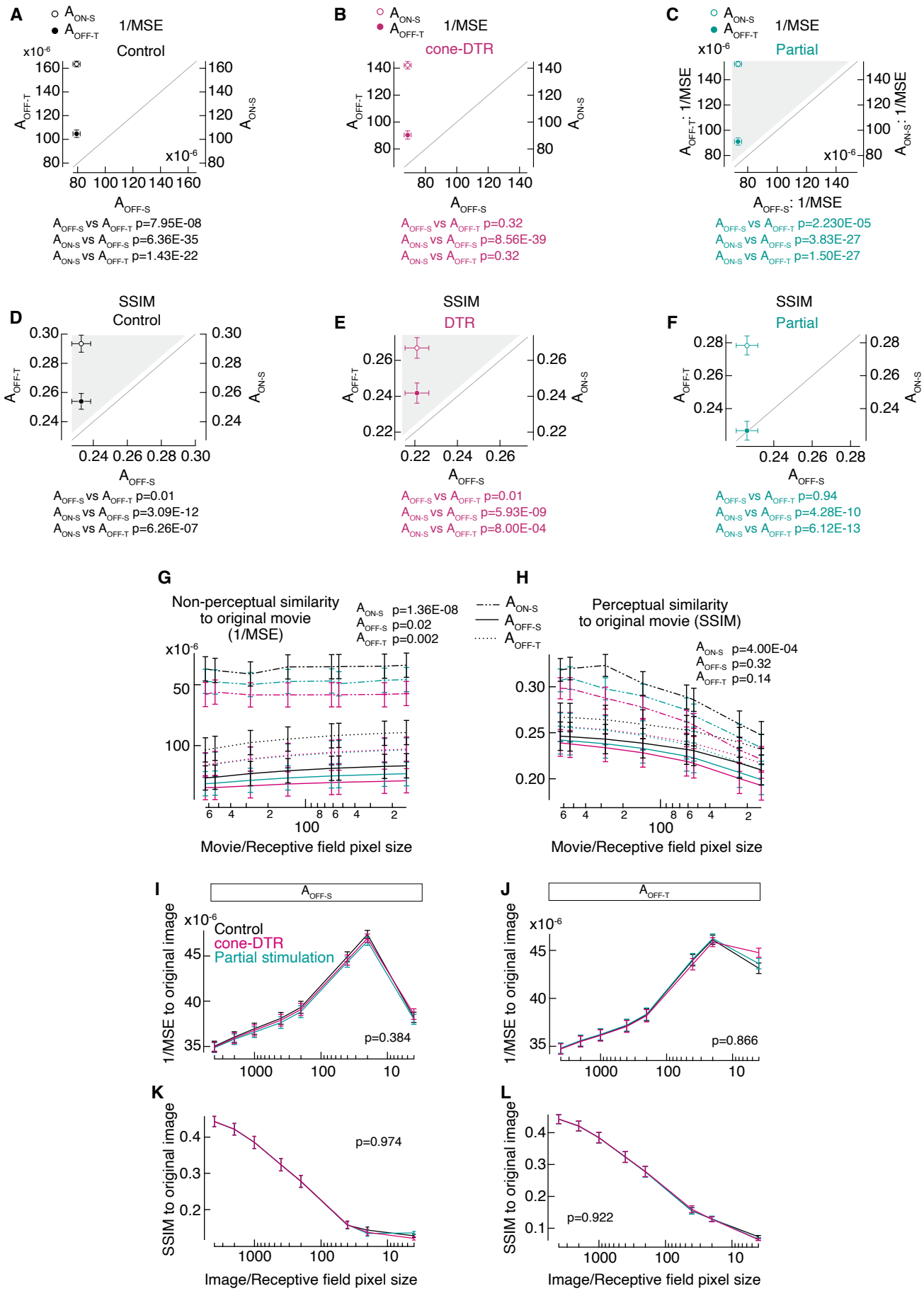
A
B
C
D
E
F
G
H
I
J
K
L
1/MSE
Control
cone-DTR
Partial
SSIM
DTR
Partial
A_{ON-S}
A_{OFF-T}
A_{OFF-S}
A_{OFF-S} vs A_{OFF-T} p=7.95E-08
A_{ON-S} vs A_{OFF-S} p=6.36E-35
A_{ON-S} vs A_{OFF-T} p=1.43E-22
A_{OFF-S} vs A_{OFF-T} p=0.32
A_{ON-S} vs A_{OFF-S} p=8.56E-39
A_{ON-S} vs A_{OFF-T} p=0.32
A_{OFF-S} vs A_{OFF-T} p=2.230E-05
A_{ON-S} vs A_{OFF-S} p=3.83E-27
A_{ON-S} vs A_{OFF-T} p=1.50E-27
A_{OFF-S} vs A_{OFF-T} p=0.01
A_{ON-S} vs A_{OFF-S} p=3.09E-12
A_{ON-S} vs A_{OFF-T} p=6.26E-07
A_{OFF-S} vs A_{OFF-T} p=0.01
A_{ON-S} vs A_{OFF-S} p=5.93E-09
A_{ON-S} vs A_{OFF-T} p=8.00E-04
A_{OFF-S} vs A_{OFF-T} p=0.94
A_{ON-S} vs A_{OFF-S} p=4.28E-10
A_{ON-S} vs A_{OFF-T} p=6.12E-13
Non-perceptual similarity to original movie (1/MSE)
A_{ON-S} p=1.36E-08
A_{OFF-S} p=0.02
A_{OFF-T} p=0.002
Perceptual similarity to original movie (SSIM)
A_{ON-S} p=4.00E-04
A_{OFF-S} p=0.32
A_{OFF-T} p=0.14
Movie/Receptive field pixel size
1/MSE to original image
SSIM to original image
Control
cone-DTR
Partial stimulation
p=0.384
p=0.866
p=0.974
p=0.922
Image/Receptive field pixel size

Figure S6. Natural movies and images filtered by the measured spatiotemporal receptive fields following partial cone loss are perceptually similar to those filtered by control retina. (A-F) Non-perceptual similarity index (1/MSE) (A-C) and structural similarity index (SSIM) (D-F) of convolved movies in a pairwise comparison between $A_{ON\text{-}S}$ vs. $A_{OFF\text{-}T}$ vs. $A_{OFF\text{-}S}$ ganglion cells under (A, D) control, (B, E) partial stimulation, and (C, F) cone-DTR conditions. (G-H) P-values indicate differences between convolved movies with reference movies from control, cone-DTR, and partial conditions across movie dimensions in a two-way ANOVA test within each cell type for (G) 1/MSE and (H) SSIM. (I-L) 1/MSE (I-J) and structural similarity index (K-L) of convolved images as a function of image-to-receptive-field pixel ratio. P-values from two-way ANOVA to compare differences between convolved images and reference images across conditions. See also Dataset S1.